Front. Mech. Eng. 2024, 19(1): 5
https://doi.org/10.1007/s11465-023-0778-7

RESEARCH ARTICLE

Novel modular quasi-zero stiffness vibration isolator with high linearity and integrated fluid damping

Wei ZHANG[a,b], Jixing CHE[a,b], Zhiwei HUANG[a,b], Ruiqi GAO[a,b], Wei JIANG[a,b], Xuedong CHEN[a,b], Jiulin WU (✉)[a,b]

[a] *State Key Laboratory of Intelligent Manufacturing Equipment and Technology, Huazhong University of Science and Technology, Wuhan 430074, China*
[b] *School of Mechanical Science and Engineering, Huazhong University of Science and Technology, Wuhan 430074, China*
✉ *Corresponding author. E-mail: wujl@hust.edu.cn (Jiulin WU)*

ABSTRACT Passive vibration isolation systems have been widely applied due to their low power consumption and high reliability. Nevertheless, the design of vibration isolators is usually limited by the narrow space of installation, and the requirement of heavy loads needs the high supporting stiffness that leads to the narrow isolation frequency band. To improve the vibration isolation performance of passive isolation systems for dynamic loaded equipment, a novel modular quasi-zero stiffness vibration isolator (MQZS-VI) with high linearity and integrated fluid damping is proposed. The MQZS-VI can achieve high-performance vibration isolation under a constraint mounted space, which is realized by highly integrating a novel combined magnetic negative stiffness mechanism into a damping structure: The stator magnets are integrated into the cylinder block, and the moving magnets providing negative-stiffness force also function as the piston supplying damping force simultaneously. An analytical model of the novel MQZS-VI is established and verified first. The effects of geometric parameters on the characteristics of negative stiffness and damping are then elucidated in detail based on the analytical model, and the design procedure is proposed to provide guidelines for the performance optimization of the MQZS-VI. Finally, static and dynamic experiments are conducted on the prototype. The experimental results demonstrate the proposed analytical model can be effectively utilized in the optimal design of the MQZS-VI, and the optimized MQZS-VI broadened greatly the isolation frequency band and suppressed the resonance peak simultaneously, which presented a substantial potential for application in vibration isolation for dynamic loaded equipment.

KEYWORDS vibration isolation, quasi-zero stiffness, damping, magnetic spring, integrated design

1 Introduction

Vibration from the internal disturbance sources and the external environment can substantially impair the service performance of precision equipment mounted on moving carriers (such as aircraft, ships, and cars). With the improvement of accuracy in this kind of dynamic loaded precision equipment, the demand for its high-performance vibration isolation has become increasingly critical [1–4].

The related research has attracted more attention in recent years. Dong et al. [5] designed a novel passive airborne photoelectric quasi-zero stiffness (QZS) platform and introduced the friction damping such that the low-frequency vibrations can be effectively isolated, but the negative stiffness mechanism included was composed of a couple of ring magnets, which had a narrow linear region. Jiang et al. [6] proposed a three-degree-of-freedom (3-DOF) parallel stabilization platform to offset the disturbance in the vertical and horizontal directions with an adaptive compliance control strategy, which provided further applicability in marine operations or airborne filming. Liu et al. [7] proposed a method for the dynamic response and time-variant reliability analysis of an eight-rod shock isolator to improve the shock resistance performance of shipboard equipment. Shin et al. [8] developed an active mount combined with a passive rubber mount and an electromagnetic actuator and applied it in naval shipboard equipment. Qu et al. [9] established the nonlinear dynamic model of a parallel air spring

Received July 19, 2023; accepted November 19, 2023

vibration isolation system and investigated its vibration isolation characteristics with an equal height control strategy, which is a potentially useful method for the transportation of precision equipment. Li et al. [10] proposed a semiactively controlled QZS vibration isolator with a magnetorheological damper for the vibration isolation of vehicle-mounted equipment, which decreased vibration by over 70%. To sum up, isolating vibration for dynamic loaded equipment depends mostly on active vibration isolators, which have satisfactory performance, but the systems are complex with prohibitive costs and larger volume. Passive vibration isolators are also used with narrow isolating bandwidth with compact structure, low power consumption, and high reliability. Therefore, isolation methods that combine the advantages of passive and active vibration isolators (compactness, high linearity, and wide isolation frequency band) need to be developed to serve the vibration isolation of dynamic loaded equipment better.

To broaden the isolation frequency bandwidth of the passive isolation system, negative stiffness mechanisms are proposed to counteract the positive stiffness at the equilibrium state of the payload [11–13]. Combining the negative stiffness mechanism with the positive stiffness structure can realize QZS characteristics, which resolve the contradiction between high load capacity and low-frequency isolation ability. Earnest efforts have been made, and various QZS vibration isolators have been proposed [14–16]. Two kinds of QZS vibration isolators are commonly applied to dynamic loaded equipment [17, 18]. The first type is composed of the positive stiffness elastic element with a special geometric distribution. Jing et al. [19] proposed an efficient stiffness-manipulation method using a flexible, compact X-shaped structure including simplicity and efficiency in manufacturing and assembly. Abuabiah et al. [20] designed a compact QZS vibration isolator that consisted of a vertical spring and a pair of oblique springs equipped with a horizontal adjustment mechanism, which could be fitted for small cars to provide good comfort for the driver and passengers. Zhao et al. [21,22] proposed a new limb-like QZS system with two or three pairs of oblique springs to enlarge the QZS region, which performed better than the corresponding QZS system with one pair of oblique springs. Wei [23] designed a novel vehicle-mounted QZS vibration isolator, which had a satisfactory vibration isolation effect for large excitation from the road. Chen et al. [24] proposed a QZS vibration isolator combined with oblique springs to solve the problem of passive broadband vibration isolation for vehicle-mounted moving platform optic–electronic equipment, which can achieve a 90% isolation efficiency in the range of 20–2000 Hz. The second type of QZS vibration isolator was realized by paralleling the magnetic negative stiffness mechanism (MNSM) with the positive stiffness spring. Its performance of vibration isolation mainly depended on the MNSM, and the region of the QZS was varied by adjusting the structural parameters [25,26]. Zhang et al. [27] proposed a compact magnetic Halbach high negative stiffness isolator that contributed to light-weight design and facilitated low-frequency vibration isolation. Yuan et al. [28] proposed a vibration isolator based on a tunable negative stiffness mechanism combining the advantages of high-static–low-dynamic stiffness isolators to expand the isolation frequency band and variable stiffness isolators to suppress resonance. Tu et al. [29] employed a couple of columnar magnets with a specific arrangement to design a negative stiffness magnetic spring, reduced the resonance frequency vibration. The moving and static magnets of MNSM had parallel directions of magnetization in most studies [30–33], and research on the negative stiffness mechanism composed of stator and moving magnets with orthogonal magnetization directions is limited, especially in composite configurations that combine attractive magnetic couples and repel magnetic couples [34,35].

In addition, the modular quasi-zero stiffness vibration isolator (MQZS-VI) is mostly realized by this method, which is a kind of high-interchangeability QZS vibration isolator that is the key part of multiple-DOF vibration isolation platform. Zheng et al. [36] proposed an MQZS-VI by employing a pair of magnets with radiative magnetization and built a Stewart platform to extend the isolation frequency band, which had a satisfactory performance. However, the nonlinear behavior of the MQZS-VI was serious. Hao et al. [37] established an MQZS-VI with electromagnetic spring to realize adjustable QZS, which could suppress the low-frequency vibration of high-precision instruments better. Hao et al. [38] also proposed an MQZS-VI with a couple of magnets with axial magnetization to build a 6-DOF vibration isolation system that provided a promising approach to suppress multidirectional shock vibration. Although the existing MQZS-VIs have a wider isolation frequency band, the isolators have no damping structure and the nonlinear behavior is noticeable.

Therefore, integrating the damping structure into the MQZS-VI is necessary, which plays a remarkable role in vibration isolation for dynamic loaded equipment [39–41]. Earnest efforts in damping have been made, and various damping structures have been proposed to establish the vibration isolator [42–45]. Ma et al. [46] proposed two types of nonlinear electromagnetic shunt damping that have similar vibration suppression performance in the resonance region more effectively than the traditional linear electromagnetic one. Ma et al. [47] proposed a novel inertia damper dubbed rotational inertia damper to control the vibrations of offshore platforms, which has a good capacity for energy dissipation. Most of the above typical dampers have a superior performance in energy dissipation, but the volume of these dampers in parallel with stiffness elements is immense, which is unsuitable

for the occasion with narrow mounting space by using them. By contrast, the magnetic negative stiffness damper (MNSD) could overcome this deficiency [48]. Liu and Lui [49] proposed a mathematical model of MNSD and conducted the related parametric study. Wang et al. [50] proposed a novel passive control device termed magnetic negative stiffness eddy-current inertial mass damper for cable vibration mitigation, which integrated the advantages of the MNSD and the inertial mass damper. Although the volume of MNSDs is compact because they do not add extra stiffness elements to the system, matching the proper parameters of stiffness and damping simultaneously is challenging. Moreover, the linear interval of negative stiffness of MNSDs is rarely studied, but this index is also essential to vibration isolation for dynamic loaded equipment. Consequently, new methods that integrate the negative stiffness mechanism with high linearity (wide interval of linear stiffness) and damping structure in a compact space need to be developed, ensuring a wide interval of linear stiffness and reducing the complexity of matching dynamic parameters simultaneously.

To improve the performance of passive isolation systems used for dynamic loaded equipment with constraint mounting space, a novel MQZS-VI with high linearity and integrated fluid damping is proposed in this paper, in which both possess the modularity, large damping, and QZS characteristics. The proposed MQZS-VI is realized by highly integrating the novel combined magnetic negative stiffness mechanism (CMNSM) into the damping structure: The stator magnet is integrated into the cylinder block, and the moving magnet providing negative-stiffness force also acts as the piston supplying damping force simultaneously. Given its integrated configuration, the MQZS-VI is compact and possesses a certain impact resistance. The MQZS-VI has a wider QZS interval than the QZS vibration isolator with typical CMNSM, and the negative stiffness and damping coefficient of MQZS-VI can be matched independently due to the decoupling of fluid field and magnetic field compared with traditional MNSD. In addition, the modular design method is adopted to improve the interchangeability of MQZS-VI, which can be utilized in groups to establish multiple-DOF platforms to isolate vibration.

This paper is organized as follows. In Section 2, the schematic model of the MQZS-VI is presented, and the analytical model of the novel CMNSM is established and verified. In Section 3, the effects of the geometric parameters on the stiffness and damping characteristics of the MQZS-VI are revealed, and the design procedure and advantages are demonstrated. In Section 4, experiments are conducted and verified. In Section 5, the conclusions and prospects are drawn.

2 Concept and modeling of the MQZS-VI

2.1 Structure description

Figure 1 shows the proposed MQZS-VI can be used to build the Stewart platform to isolate vibration for dynamic loaded equipment. The MQZS-VI comprises the novel CMNSM, metal spring, and damping element. The key part of the MQZS-VI is the novel CMNSM that generates axial negative stiffness, which consists of ring magnets with different magnetization directions. The stator magnets are fixed on the top, middle, and bottom of the cylinder block (the blue parts in Fig. 1). The middle stator magnet is magnetized radiatively, and the other stator magnets are magnetized axially. The moving magnets are assembled at the end of the piston rod (the green parts in Fig. 1), and the directions of magnetization for the top–bottom moving magnets are the same as those for the top–bottom stator magnets. The middle moving magnet is magnetized radiatively but opposite to the middle stator magnet. All the specific magnetization directions of magnets are marked with black arrows in

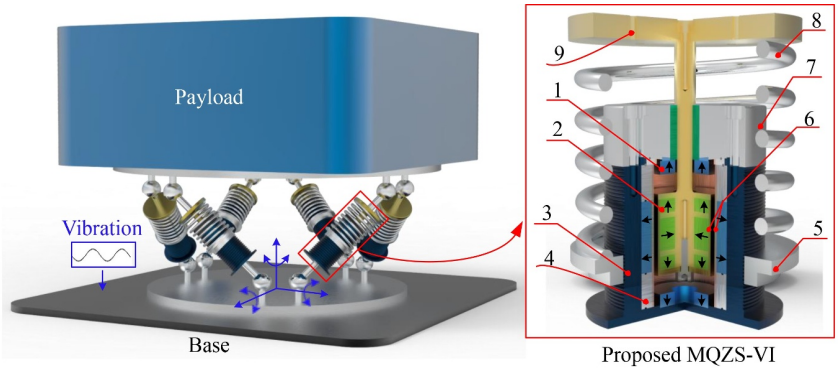

Fig. 1 Schematic of the proposed modular quasi-zero stiffness vibration isolator (MQZS-VI). 1–Stator magnet, 2–Moving magnet, 3–Cylinder block, 4–Positioning bushing, 5–Adjustable base, 6–Annular sleeve, 7–End cover, 8–Metal spring, 9–Piston rod.

Fig. 1. The metal spring connecting the piston rod and the adjustable base is designed to support the payload. To guarantee the middle position of the stator magnet with radiative magnetization, the positioning bushings are installed on both sides. Moreover, the annular sleeves are designed to assemble the ring magnets with radiative magnetization and to narrow the damping gap. Consequently, the MQZS-VI possesses QZS and damping characteristics simultaneously, which can be applied to diverse occasions by matching various joints as a modular part in the vibration isolating system.

Figure 2(a) defines the geometric parameters of the MQZS-VI. To investigate the effect of geometric parameters on stiffness characteristics conveniently, parts of the parameters are designed to be equal. The geometric dimensions of the moving magnets on the top–bottom side as well as those of the stator magnets on the top–bottom side are equivalent. H_0 and H_3 represent the axial length of the moving magnets and the stator magnets on the top–bottom side, respectively, and their thicknesses are denoted as T_1 and T_3, respectively. The thickness of the moving magnet in the middle is also T_1. All the moving magnets have the same inner radius r_i, which also denotes the inner radius of the stator magnets on the top–bottom side. The critical parameters also include the thickness of the middle stator magnet T_2, radial gap between the moving magnets and middle stator magnet λ, axial gap between the moving magnets and stator magnets on the top–bottom side L, the axial length of the middle stator magnet H_2, and the axial length of the assemble moving magnet H_1. The distance between the middle moving magnet and the top–bottom moving magnets is ι, which indicates the inside gap of moving magnets in this paper. Figure 2(b) shows the damping gap δ is smaller than the radial gap λ due to the existence of annular sleeves; the radius and height of the piston head are R_p and H_p, respectively.

2.2 Analytical model of the novel CMNSM

Although many basic methods have been proposed to calculate the axial force of ring magnetic bearings or couplings [51–55], no direct way exists for calculating the axial force of this CMNSM with such a configuration of ring magnets, which contain axial and radiative magnetization simultaneously. Hence, the analytical model to calculate the axial force is proposed and established based on the magnetic charge method and ampere–current model in this paper. Assuming uniform magnetization, the axially magnetized magnets are equivalent to a couple of current loops in opposite directions, while ring magnets with radiative magnetization are equal to the surface and volume magnetic charges. Thus, the magnets with axial magnetization are discretized to current loops, and the magnets with radiative magnetization are discretized to magnetic charge loops.

Before calculating the axial force of this CMNSM, the expression of the composite magnetic field of arbitrary point generated by all the current loops and magnetic charge loops is obtained, and the related derivations are based on Refs. [54,55]. Therefore, the related calculation result is given directly. The magnetic flux density generated by the magnetic charge loop $\boldsymbol{B}^{\mathrm{q}}$ at arbitrary point in space is

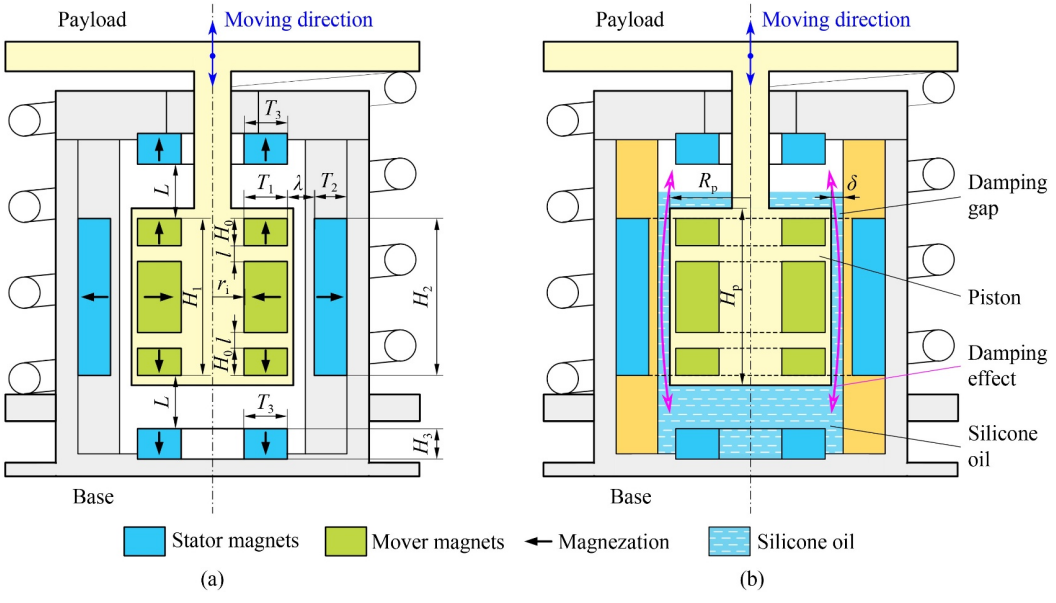

Fig. 2 Configuration of the modular quasi-zero stiffness vibration isolator: distribution of geometric parameters (a) that affect negative stiffness and (b) that affect damping coefficient.

$$\begin{aligned}
&\boldsymbol{B}^{\mathrm{q}}(r_{\mathrm{m}},z_{\mathrm{m}},r_{\mathrm{s}},z_{\mathrm{s}})=\boldsymbol{B}_{\mathrm{r}}^{\mathrm{q}}(r_{\mathrm{m}},z_{\mathrm{m}},r_{\mathrm{s}},z_{\mathrm{s}})+\boldsymbol{B}_{z}^{\mathrm{q}}(r_{\mathrm{m}},z_{\mathrm{m}},r_{\mathrm{s}},z_{\mathrm{s}})\\
&=B_{\mathrm{r}}^{\mathrm{q}}(r_{\mathrm{m}},z_{\mathrm{m}},r_{\mathrm{s}},z_{\mathrm{s}})\boldsymbol{r}+B_{z}^{\mathrm{q}}(r_{\mathrm{m}},z_{\mathrm{m}},r_{\mathrm{s}},z_{\mathrm{s}})\boldsymbol{z}\\
&=\frac{\mu_0 Q_{\mathrm{s}}}{2\pi^2}\left[\frac{\left(r_{\mathrm{m}}^2-r_{\mathrm{s}}^2-(z_{\mathrm{m}}-z_{\mathrm{s}})^2\right)E\left(\frac{\pi}{2},r_{\mathrm{m}},z_{\mathrm{m}},r_{\mathrm{s}},z_{\mathrm{s}}\right)}{2r_{\mathrm{m}}D_1(r_{\mathrm{m}},z_{\mathrm{m}},r_{\mathrm{s}},z_{\mathrm{s}})\sqrt{D_2(r_{\mathrm{m}},z_{\mathrm{m}},r_{\mathrm{s}},z_{\mathrm{s}})}}\right.\\
&\left.+\frac{G\left(\frac{\pi}{2},r_{\mathrm{m}},z_{\mathrm{m}},r_{\mathrm{s}},z_{\mathrm{s}}\right)}{2r_{\mathrm{m}}\sqrt{D_2(r_{\mathrm{m}},z_{\mathrm{m}},r_{\mathrm{s}},z_{\mathrm{s}})}}\right]\boldsymbol{r}\\
&+\frac{\mu_0 Q_{\mathrm{s}}}{2\pi^2}\frac{(z_{\mathrm{m}}-z_{\mathrm{s}})E\left(\frac{\pi}{2},r_{\mathrm{m}},z_{\mathrm{m}},r_{\mathrm{s}},z_{\mathrm{s}}\right)}{D_1(r_{\mathrm{m}},z_{\mathrm{m}},r_{\mathrm{s}},z_{\mathrm{s}})\sqrt{D_2(r_{\mathrm{m}},z_{\mathrm{m}},r_{\mathrm{s}},z_{\mathrm{s}})}}\boldsymbol{z}\\
&=Q_{\mathrm{s}}P_{\mathrm{r}}^{\mathrm{q}}(r_{\mathrm{m}},z_{\mathrm{m}},r_{\mathrm{s}},z_{\mathrm{s}})\boldsymbol{r}+Q_{\mathrm{s}}P_{z}^{\mathrm{q}}(r_{\mathrm{m}},z_{\mathrm{m}},r_{\mathrm{s}},z_{\mathrm{s}})\boldsymbol{z},
\end{aligned}\tag{1}$$

where

$$\begin{cases}
D_1(r_{\mathrm{m}},z_{\mathrm{m}},r_{\mathrm{s}},z_{\mathrm{s}})=(r_{\mathrm{m}}-r_{\mathrm{s}})^2+(z_{\mathrm{m}}-z_{\mathrm{s}})^2,\\
D_2(r_{\mathrm{m}},z_{\mathrm{m}},r_{\mathrm{s}},z_{\mathrm{s}})=(r_{\mathrm{m}}+r_{\mathrm{s}})^2+(z_{\mathrm{m}}-z_{\mathrm{s}})^2,\\
E\left(\frac{\pi}{2},r_{\mathrm{m}},z_{\mathrm{m}},r_{\mathrm{s}},z_{\mathrm{s}}\right)=\int_0^{\frac{\pi}{2}}\sqrt{1-\frac{4r_{\mathrm{m}}r_{\mathrm{s}}\sin^2\psi}{D_2(r_{\mathrm{m}},z_{\mathrm{m}},r_{\mathrm{s}},z_{\mathrm{s}})}}\,\mathrm{d}\psi,\\
G\left(\frac{\pi}{2},r_{\mathrm{m}},z_{\mathrm{m}},r_{\mathrm{s}},z_{\mathrm{s}}\right)=\int_0^{\frac{\pi}{2}}\frac{1}{\sqrt{1-\frac{4r_{\mathrm{m}}r_{\mathrm{s}}\sin^2\psi}{D_2(r_{\mathrm{m}},z_{\mathrm{m}},r_{\mathrm{s}},z_{\mathrm{s}})}}}\mathrm{d}\psi,
\end{cases}\tag{2}$$

$\boldsymbol{B}_{\mathrm{r}}^{\mathrm{q}}$ and $\boldsymbol{B}_{z}^{\mathrm{q}}$ are the radial and axial magnetic flux density generated by the magnetic charge loop, $B_{\mathrm{r}}^{\mathrm{q}}$ and B_{z}^{q} are the magnitude of the radial and axial magnetic flux density generated by the magnetic charge loop, respectively, superscript "q" indicates that the physical quantity is related to the magnetic charge loop, $\boldsymbol{r}$ and $\boldsymbol{z}$ are the radial and axial unit vector, r_{s} and z_{s} represent the radius and axial coordinate of micro units of equivalent loops of the stator magnet, r_{m} and z_{m} represent the radius and axial coordinate of micro units of equivalent loops of the moving magnet, E and G are complete elliptic integral of the second kind and first kind respectively, and ψ is the variable of integration. Similarly, the magnetic flux density generated by the equivalent current loop $\boldsymbol{B}^{\mathrm{c}}$ at arbitrary point in space consists of the radial and axial magnetic flux density generated by the equivalent current loop $\boldsymbol{B}_{\mathrm{r}}^{\mathrm{c}}$ and $\boldsymbol{B}_{z}^{\mathrm{c}}$, which is

$$\begin{aligned}
&\boldsymbol{B}^{\mathrm{c}}=(r_{\mathrm{m}},z_{\mathrm{m}},r_{\mathrm{s}},z_{\mathrm{s}})=\boldsymbol{B}_{\mathrm{r}}^{\mathrm{c}}(r_{\mathrm{m}},z_{\mathrm{m}},r_{\mathrm{s}},z_{\mathrm{s}})+\boldsymbol{B}_{z}^{\mathrm{c}}(r_{\mathrm{m}},z_{\mathrm{m}},r_{\mathrm{s}},z_{\mathrm{s}})\\
&=B_{\mathrm{r}}^{\mathrm{c}}(r_{\mathrm{m}},z_{\mathrm{m}},r_{\mathrm{s}},z_{\mathrm{s}})\boldsymbol{r}+B_{z}^{\mathrm{c}}(r_{\mathrm{m}},z_{\mathrm{m}},r_{\mathrm{s}},z_{\mathrm{s}})\boldsymbol{z}\\
&=\frac{\mu_0 I_{\mathrm{s}}}{2\pi r_{\mathrm{m}}}\frac{z_{\mathrm{m}}-z_{\mathrm{s}}}{\sqrt{D_2(r_{\mathrm{m}},z_{\mathrm{m}},r_{\mathrm{s}},z_{\mathrm{s}})}}\left[-G\left(\frac{\pi}{2},r_{\mathrm{m}},z_{\mathrm{m}},r_{\mathrm{s}},z_{\mathrm{s}}\right)\right.\\
&\left.+\frac{\left(r_{\mathrm{m}}^2+r_{\mathrm{s}}^2+(z_{\mathrm{m}}-z_{\mathrm{s}})^2\right)E\left(\frac{\pi}{2},r_{\mathrm{m}},z_{\mathrm{m}},r_{\mathrm{s}},z_{\mathrm{s}}\right)}{D_1(r_{\mathrm{m}},z_{\mathrm{m}},r_{\mathrm{s}},z_{\mathrm{s}})}\right]\boldsymbol{r}\\
&+\frac{\mu_0 I_{\mathrm{s}}}{2\pi}\frac{1}{\sqrt{D_2(r_{\mathrm{m}},z_{\mathrm{m}},r_{\mathrm{s}},z_{\mathrm{s}})}}\left[G\left(\frac{\pi}{2},r_{\mathrm{m}},z_{\mathrm{m}},r_{\mathrm{s}},z_{\mathrm{s}}\right)\right.\\
&\left.+\frac{\left(-r_{\mathrm{m}}^2+r_{\mathrm{s}}^2-(z_{\mathrm{m}}-z_{\mathrm{s}})^2\right)E\left(\frac{\pi}{2},r_{\mathrm{m}},z_{\mathrm{m}},r_{\mathrm{s}},z_{\mathrm{s}}\right)}{D_1(r_{\mathrm{m}},z_{\mathrm{m}},r_{\mathrm{s}},z_{\mathrm{s}})}\right]\boldsymbol{z}\\
&=I_{\mathrm{s}}P_{\mathrm{r}}^{\mathrm{c}}(r_{\mathrm{m}},z_{\mathrm{m}},r_{\mathrm{s}},z_{\mathrm{s}})\boldsymbol{r}+I_{\mathrm{s}}P_{z}^{\mathrm{c}}(r_{\mathrm{m}},z_{\mathrm{m}},r_{\mathrm{s}},z_{\mathrm{s}})\boldsymbol{z},
\end{aligned}\tag{3}$$

superscript "c" indicates that the physical quantity is related to the equivalent current loop, $B_{\mathrm{r}}^{\mathrm{c}}$ and B_{z}^{c} are the magnitude of the radial and axial magnetic flux density generated by the current loop, respectively, μ_0 is the permeability of the vacuum, Q_{s} is the value of the magnetic charge of the equivalent magnetic charge loop of the stator magnet with axial magnetization, and I_{s} is the surface current of the equivalent current loop of the stator magnet with radiative magnetization. Hence, the axial force of the magnetic charge loop F_{zq}^{q} and current loop F_{zq}^{c} of stator magnets acting on the magnetic charge loop of moving magnets can be calculated by Ref. [54]:

$$\begin{cases}
F_{zq}^{\mathrm{q}}(r_{\mathrm{m}},z_{\mathrm{m}},r_{\mathrm{s}},z_{\mathrm{s}})=Q_{\mathrm{m}}B_{z}^{\mathrm{q}}(r_{\mathrm{m}},z_{\mathrm{m}},r_{\mathrm{s}},z_{\mathrm{s}})\\
\qquad\qquad=Q_{\mathrm{m}}Q_{\mathrm{s}}P_{z}^{\mathrm{q}}(r_{\mathrm{m}},z_{\mathrm{m}},r_{\mathrm{s}},z_{\mathrm{s}}),\\
F_{zq}^{\mathrm{c}}(r_{\mathrm{m}},z_{\mathrm{m}},r_{\mathrm{s}},z_{\mathrm{s}})=Q_{\mathrm{m}}B_{z}^{\mathrm{c}}(r_{\mathrm{m}},z_{\mathrm{m}},r_{\mathrm{s}},z_{\mathrm{s}})\\
\qquad\qquad=Q_{\mathrm{m}}Q_{\mathrm{s}}P_{z}^{\mathrm{c}}(r_{\mathrm{m}},z_{\mathrm{m}},r_{\mathrm{s}},z_{\mathrm{s}}).
\end{cases}\tag{4}$$

Similarly, the axial force of the magnetic charge loop F_{zc}^{q} and current loop F_{zc}^{c} of stator magnets acting on the current loop of moving magnets can be obtained by Ref. [55]:

$$\begin{cases}
F_{zc}^{\mathrm{q}}(r_{\mathrm{m}},z_{\mathrm{m}},r_{\mathrm{s}},z_{\mathrm{s}})=2\pi r_{\mathrm{m}}I_{\mathrm{m}}B_{\mathrm{r}}^{\mathrm{q}}(r_{\mathrm{m}},z_{\mathrm{m}},r_{\mathrm{s}},z_{\mathrm{s}})\\
\qquad\qquad=2\pi r_{\mathrm{m}}I_{\mathrm{m}}I_{\mathrm{s}}P_{\mathrm{r}}^{\mathrm{q}}(r_{\mathrm{m}},z_{\mathrm{m}},r_{\mathrm{s}},z_{\mathrm{s}}),\\
F_{zc}^{\mathrm{c}}(r_{\mathrm{m}},z_{\mathrm{m}},r_{\mathrm{s}},z_{\mathrm{s}})=2\pi r_{\mathrm{m}}I_{\mathrm{m}}B_{\mathrm{r}}^{\mathrm{c}}(r_{\mathrm{m}},z_{\mathrm{m}},r_{\mathrm{s}},z_{\mathrm{s}})\\
\qquad\qquad=2\pi r_{\mathrm{m}}I_{\mathrm{m}}I_{\mathrm{s}}P_{\mathrm{r}}^{\mathrm{c}}(r_{\mathrm{m}},z_{\mathrm{m}},r_{\mathrm{s}},z_{\mathrm{s}}),
\end{cases}\tag{5}$$

where Q_{m} is the magnetic charge of the equivalent magnetic charge loop of moving magnet with axial magnetization, and I_{m} is the surface current of the equivalent current loop of moving magnet with radiative magnetization.

After obtaining the expression of composite magnetic force, with regard to the micro units of the magnetic charge loop and current loop, the values of magnetic charge or current and their coordinates should be calculated. Figure 3 shows that for the radially magnetized magnets, the following formulas are satisfied:

$$\begin{cases}
\boldsymbol{n}_1\cdot\boldsymbol{M}_1=M_1,\ \boldsymbol{n}_2\cdot\boldsymbol{M}_1=-M_1,\\
\boldsymbol{n}_3\cdot\boldsymbol{M}_2=-M_2,\ \boldsymbol{n}_4\cdot\boldsymbol{M}_2=-M_2,\\
\mathrm{div}\boldsymbol{M}_1=-\dfrac{M_1}{r_{vp}},\ \mathrm{div}\boldsymbol{M}_2=\dfrac{M_2}{r_{vk}},
\end{cases}\tag{6}$$

where r_{vp} and r_{vk} are the radii of the equivalent volume fictitious magnetic charge loops of the middle moving magnet and the stator magnet, respectively. The boundary conditions of the axially magnetized magnets are

$$\begin{cases}
\boldsymbol{M}_3\times\boldsymbol{n}_5=\boldsymbol{J}_1=-M_3\boldsymbol{\theta},\ \boldsymbol{M}_3\times\boldsymbol{n}_6=\boldsymbol{J}_2=M_3\boldsymbol{\theta},\\
\boldsymbol{M}_4\times\boldsymbol{n}_7=\boldsymbol{J}_3=M_4\boldsymbol{\theta},\ \boldsymbol{M}_4\times\boldsymbol{n}_8=\boldsymbol{J}_4=-M_3\boldsymbol{\theta},
\end{cases}\tag{7}$$

where $\boldsymbol{M}_i$ (i = 1,2,…,4) is the magnetization of the magnet, M_i (i = 1,2,…,4) is the magnitude of the magnetization of the magnet, $\boldsymbol{\theta}$ is the circumferential unit vector, and $\boldsymbol{n}_k$ (k = 1,2,…,8) is the unit vector normal to the surface, and $\boldsymbol{J}_l$ (l = 1,2,…,4) is the surface density of the equivalent ampere's currents. z_p (p = 1,2,…,6) is the

axial coordinate of the lower plane of each magnet, which can be seen in Fig. 3.

The discretizing model of this CMNSM is shown in Fig. 4. The magnets with radiative magnetization are equivalent to surface magnetic charge loops and volume magnetic charge loops, and the magnets with axial magnetization are equivalent to current loops. For the micro unit of equivalent inner surface magnetic charge loop of the middle moving magnet, Q_{s1} is the magnetic charge and Q_{s2} is the magnetic charge of the micro unit of the related outer surface. For the micro unit of the equivalent inner surface magnetic charge loop of the middle stator magnet, Q_{s3} is the magnetic charge and Q_{s4} is the magnetic charge of the micro unit of the related outer surface. Q_{v1} is the magnetic charge of micro unit of equivalent volume magnetic charge loops of the middle moving magnet and Q_{v2} represents that of the stator magnet. Subscripts "s" and "v" indicate that these parameters are related to the surface magnetic charge loop and the volume magnetic charge loop, respectively. For the micro unit of equivalent current loops of top–bottom moving magnets and the stator magnets, I_{1u} and I_{2u} are the currents of inner and outer circle loop of the upper moving magnet, respectively; I_{1b} and I_{2b} are the currents of inner and outer circle loop of the bottom moving magnet, respectively; I_{3u} and I_{4u} are the currents of inner and outer circle loop of the upper stator magnet, respectively; I_{3b} and I_{4b} are the currents of inner and outer circle loop of the bottom stator magnet, respectively.

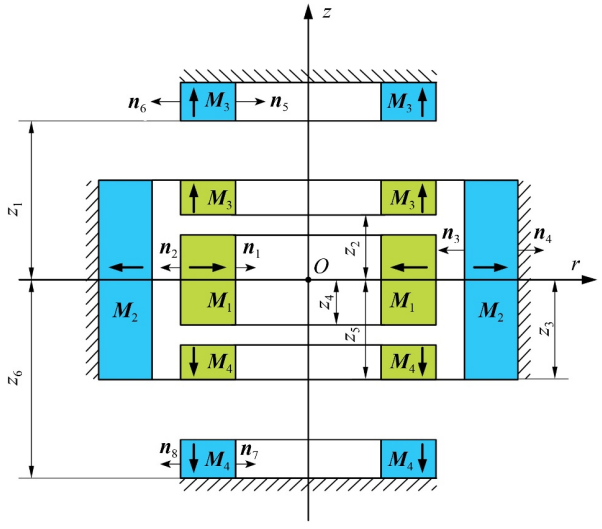

Fig. 3 Magnetization diagram of the novel combined magnetic negative stiffness mechanism.

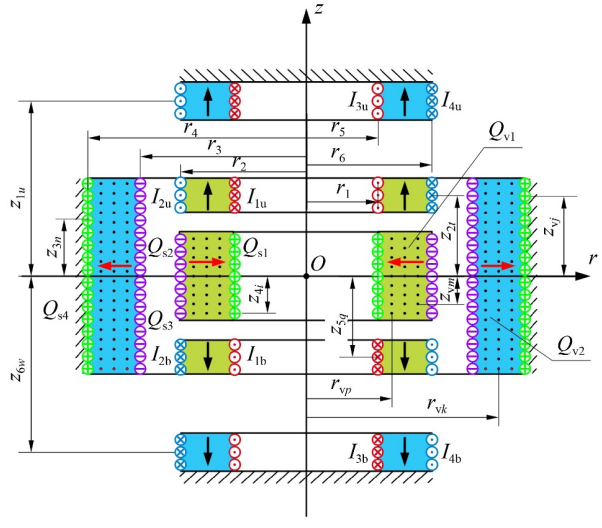

Fig. 4 Discretizing model of the novel combined magnetic negative stiffness mechanism.

The axial coordinates of the micro units of the equivalent magnetic charge loop and the current loop are shown in Fig. 4 and they are

$$\begin{cases} z_{1u} = z_1 + \dfrac{(2u_z - 1)H_3}{2N_c}, & u_z = 1,2,\ldots,N_c, \\ z_{2t} = z_2 + \dfrac{(2t_z - 1)H_0}{2N_c}, & t_z = 1,2,\ldots,N_c, \\ z_{3n} = z_3 + \dfrac{(2n_z - 1)H_2}{2N_s}, & n_z = 1,2,\ldots,N_s, \\ z_{4i} = z_4 + \dfrac{(2i_z - 1)(H_1 - 2H_0 - 2\iota)}{2N_s}, & i_z = 1,2,\ldots,N_s, \\ z_{5q} = z_5 + \dfrac{(2q_z - 1)H_0}{2N_c}, & q_z = 1,2,\ldots,N_c, \\ z_{6w} = z_6 + \dfrac{(2w_z - 1)H_3}{2N_c}, & w_z = 1,2,\ldots,N_c, \\ z_{vm} = z_4 + \dfrac{(2m_z - 1)(H_1 - 2H_0 - 2\iota)}{2N_v}, & m_z = 1,2,\ldots,N_v, \\ z_{vj} = z_3 + \dfrac{(2j_z - 1)H_2}{2N_v}, & j_z = 1,2,\ldots,N_v, \end{cases} \tag{8}$$

where N_b (b = c, v, s) are the number of segments for fictitious current loops, volume magnetic charge loops, and surface magnetic charge loops, respectively, z_1 and z_2 are axial coordinates of the lower plane of the upper stator magnet and the upper moving magnet, respectively, z_{1u} and z_{2t} are the axial coordinates of the current loop of the upper stator magnet and the upper moving magnet, respectively, z_3 and z_4 are the axial coordinates of the lower plane of the middle stator magnet and the middle moving magnet, respectively, z_{3n} and z_{4i} are the axial coordinates of the surface magnetic charge loop of the middle stator magnet and the middle moving magnet, respectively, z_5 and z_6 are the axial coordinates of the lower plane of the lower moving magnet and the lower stator magnet, respectively, and z_{5q} and z_{6w} are the axial coordinates of the current loop of the lower moving magnet and the lower stator magnet, respectively. The subscripts of axial coordinates of the micro units are set to be convenient for identifying their calculation process. Simplifying the relevant geometric parameters has no effect on the accuracy of the model, which depends on N_b.

The radius of the equivalent magnetic charge or the current loop can be presented as

$$\begin{cases} r_{vp} = r_i + \dfrac{(2p_r - 1)T_1}{2N_v},\ p_r = 1,2,\ldots,N_v, \\ r_{vk} = r_3 + \dfrac{(2k_r - 1)T_2}{2N_v},\ k_r = 1,2,\ldots,N_v, \\ r_1 = r_i,\ r_2 = r_i + T_1, \\ r_3 = r_i + T_1 + \lambda,\ r_4 = r_i + T_1 + \lambda + T_2, \\ r_5 = r_i,\ r_6 = r_i + T_3, \end{cases} \tag{9}$$

where r_1 and r_2 are inner and outer radii of the moving magnet, respectively, r_3 and r_4 are inner and outer radii of the middle stator magnet, respectively, and r_5 and r_6 are inner and outer radii of the upper stator magnet, as well as the bottom stator magnet, respectively, and r_i is the inner radius of all the magnets apart from the middle stator magnet. According to Eq. (6), the magnetic charges of the micro unit of the equivalent surface and volume magnetic charge loops can be obtained by

$$\begin{cases} Q_{s1} = 2\pi r_1 M_1 (H_1 - 2H_0 - 2\iota)/N_s, \\ Q_{s2} = -2\pi r_2 M_1 (H_1 - 2H_0 - 2\iota)/N_s, \\ Q_{s3} = -2\pi r_3 M_2 H_2/N_s, \\ Q_{s4} = 2\pi r_4 M_2 H_2/N_s, \\ Q_{v1} = -\mathrm{div}\boldsymbol{M}_1 \cdot 2\pi r_{vp}(H_1 - 2H_0 - 2\iota)T_1/N_v^2 \\ \quad\ = 2\pi(H_1 - 2H_0 - 2\iota)M_1 T_1/N_v^2 \\ Q_{v2} = -\mathrm{div}\boldsymbol{M}_2 \cdot 2\pi r_{vk} H_2 M_2 T_2/N_v^2 = -2\pi H_2 M_2 T_2/N_v^2. \end{cases} \tag{10}$$

According to Eq. (7), the micro units of equivalent current loop exist on the inner and outer axially magnetized magnet surfaces.

$$\begin{cases} I_{1u} = I_{3u} = J_1 H_3/N_c = -M_3 H_3/N_c, \\ I_{2u} = I_{4u} = J_2 H_3/N_c = M_3 H_3/N_c, \\ I_{1b} = I_{3b} = J_3 H_3/N_c = M_4 H_3/N_c, \\ I_{2b} = I_{4b} = J_4 H_3/N_c = -M_4 H_3/N_c. \end{cases} \tag{11}$$

In this paper, the moving magnets consist of three parts: the top moving magnet, the middle moving magnet, and the lower moving magnet. The axial force of this CMNSM also is divided into three parts for calculation. After quantifying the forces of the three stators on the moving magnets, the final axial force is obtained by summing them. The axial force and stiffness of CMNSM can be obtained by

$$\begin{cases} F_z(z) = F_z^{u}(z) + F_z^{m}(z) + F_z^{l}(z), \\ k_z(z) = -\dfrac{\mathrm{d}F_z(z)}{\mathrm{d}z}, \end{cases} \tag{12}$$

where z denotes the relative axial displacement, and F_z^* (* = u, m, l) represent the axial force of moving magnets suffered from the top stator, the middle stator, and the lower stator, respectively. The subscript "z" indicates the direction of this parameter is axial. Specific expressions are listed in the Electronic Supplementary Material.

To simplify the calculation, the axial stiffness is finally obtained by the calculus of differences according to the derived analytical solutions of the axial force of the CMNSM. In addition, the finite element software (COMSOL Multiphysics 5.6) is employed to obtain the force–displacement and stiffness–displacement curves. The consistency of related curves between the finite element analysis (FEA) solution and the analytical solution are compared to validate the correctness of the analytical model. All the parameters of the CMNSM between the FEA model and analytical model are set identically, and the method of 3D rotating body modeling is utilized to speed up the finite element calculation greatly, as shown in Fig. 5(a). The simulated axial force and negative stiffness are presented in Fig. 5(b) and compared with the analytical solutions. The results achieved by these two methods agree, and the curve of the negative stiffness is symmetric about the equilibrium

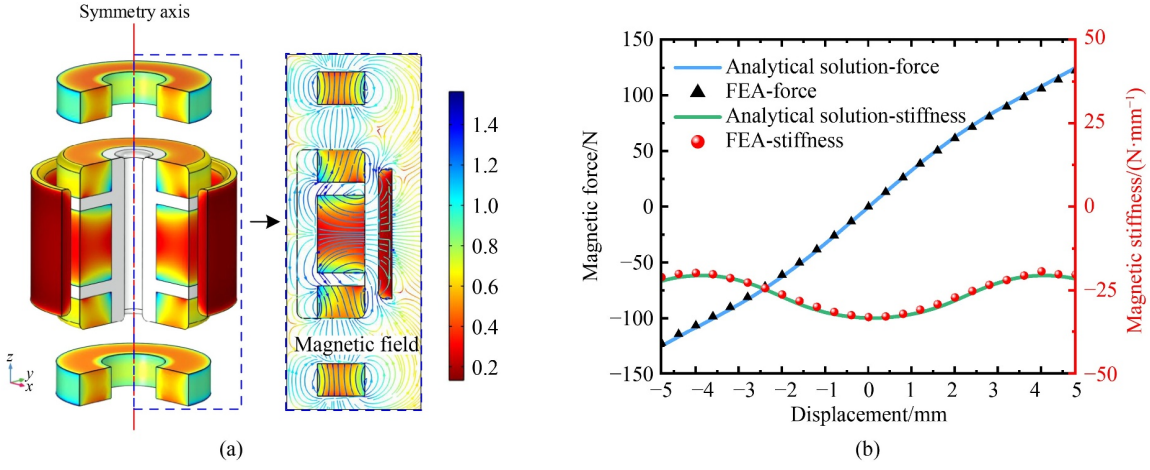

Fig. 5 Analytical and finite element analysis (FEA) solution of the novel combined magnetic negative stiffness mechanism: (a) FEA model and (b) comparison of magnetic force and stiffness. Residual magnetic flux density B_r = 1.4 T, $T_1 = T_3$ = 7 mm, λ = 2 mm, T_2 = 2 mm, L = 7 mm, H_1 = 26 mm, H_2 = 20 mm, $H_0 = H_3$ = 5 mm, ι = 2 mm, and r_i = 5 mm.

position, which is predictable due to the symmetry of the configuration of magnets.

3 Parametric study on the characteristics of the MQZS-VI

To optimize the design of the proposed MQZS-VI, parametric studies on the negative stiffness and damping characteristics are conducted in this section. To facilitate the study on stiffness characteristic, the proposed CMNSM is divided into two subsystems: Group-1 consists of all the moving magnets and the middle stator magnet, whereas Group-2 is composed of the stator magnets on the top and bottom sides and all the moving magnets. Figure 6 shows the stiffness curves of the two subsystems calculated by the analytical model, and the negative stiffness of the CMNSM obtained by summing that of the two subsystems according to magnetic field superposition principle.

The parameters that affect negative stiffness are consolidated into three categories according to the subsystem of the CMNSM. The first type of parameters mainly affects the stiffness of Group-1, which concludes the ratio of H_1 to H_2 (α_h), the ratio of T_1 to T_2 (β_h), and the radial gap (λ). Subscript "h" indicates that the compared objects are distributed along the horizontal direction. The second type of parameters comprises the ratio of H_0 to H_3 (α_v), the ratio of T_1 to T_3 (β_v), and the axial gap (L), which are related to Group-2. Subscript "v" indicates that the compared objects are distributed along the vertical direction. Moreover, the inside gap of moving magnets (ι) has an important influence on the negative stiffness of the two subsystems concurrently. Their values vary in sequence to investigate their influences on stiffness characteristics. The relative displacement between the mover and the stator can reach the millimeter level under the actual vibration condition. Thus, the studied stiffness interval is within the range of ±5 mm around the equilibrium position in this paper.

The parameters that affect the damping coefficient include damping gap (δ), kinematic viscosity (γ) of the damping fluid, radius (R_p), and the height (H_p) of the piston. When only considering the damping characteristic, the MQZS-VI can be simplified as a viscous damper of clearance because the permeability of the damping fluid (silicone oil) is the same as that of air. Nearly no coupling effect exists between the magnetic field and the flow field considering the spatial constraints of its applied scenarios, and all the geometric parameters of the CMNSM are limited to a cylindrical space to investigate. The axial height of design space H_c is 60 mm, its radius R_c is 25 mm in this paper (subscript "c" indicates that the parameter is related to constraint), and all the initial values and varying ranges of these parameters are listed in Table 1.

3.1 Effect of geometric parameters on the negative stiffness characteristic

3.1.1 Effect of the ratio α_h (Group-1)

When increasing the ratio $\alpha_h = H_1/H_2$ by decreasing H_2, the value of stiffness at the equilibrium position descends first and rises then, as shown in Fig. 7. If $\alpha_h < 1$, the stiffness curve fluctuates frequently with smaller α_h. By contrast, the shape of the curve changes between convex and concave, which means ratio α_h affects the linearity of the negative stiffness near the equilibrium position enormously. By controlling the other parameters, the wider linear interval and the large value of stiffness can be guaranteed simultaneously during the design procedure of the MQZS-VI.

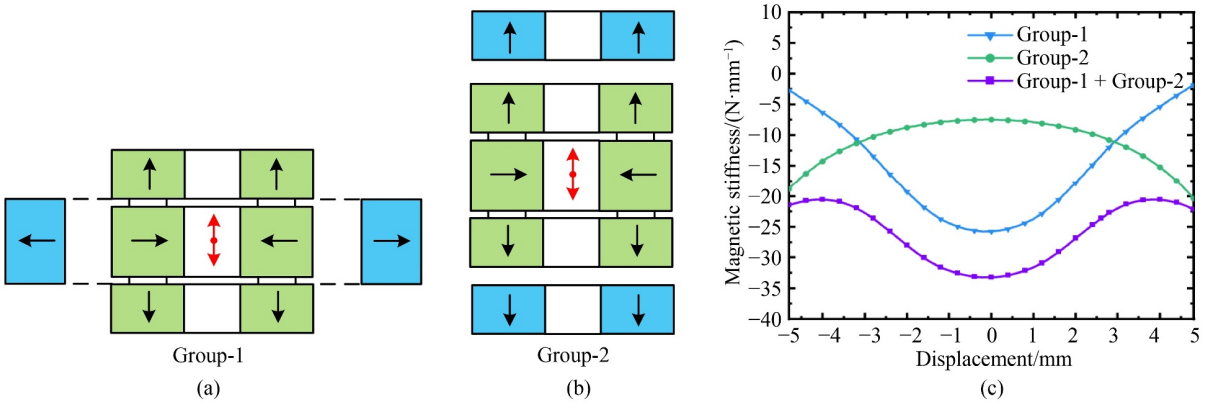

Fig. 6 Subsystems of the novel combined magnetic negative stiffness mechanism: configurations of (a) Group-1 and (b) Group-2; (c) stiffness characteristics of the subsystems. B_r = 1.4 T, $T_1 = T_3$ = 7 mm, λ = 2 mm, T_2 = 2 mm, L = 7 mm, H_1 = 26 mm, H_2 = 20 mm, $H_0 = H_3$ = 5 mm, ι = 2 mm, and r_i = 5 mm.

Table 1 Initial value and varying range of geometric parameters

Symbol	Initial value	Range	Unit
T_1	7.0	–	mm
H_1	26	–	mm
r_i	5.0	–	mm
B_r	1.4	–	T
α_h	1.0	0.6–2.6	–
β_h	3.5	0.3–4.3	–
λ	2.0	1.0–4.0	mm
α_v	1.0	0.4–2.4	–
β_v	1.0	0.4–2.4	–
L	7.0	6.0–10.0	mm
ι	2.0	0.0–4.0	mm
γ	350	350–1000	mm^2/s
H_p	28	28–35	mm
R_p	13.5	13.5–20.0	mm
δ	2.0	1.1–2.1	mm

3.1.2 Effect of the ratio of β_h (Group-1)

In this paper, the sum of T_1 and T_2 is assumed 9 mm, and $\beta_h = T_1/T_2$ varies by changing the two thickness parameters simultaneously. Figure 8(a) describes the effect of β_h on the stiffness characteristic, which indicates it is effective in improving the negative stiffness by increasing this parameter, but this effect is weakened rapidly with the increase of β_h. Moreover, the discrepancy of negative stiffness between different positions would be reduced with the decrease of this parameter, that is, the linearity of negative stiffness is also affected by this parameter, as shown in Fig. 8(b). Overall, the effect of β_h on the stiffness magnitude is more conspicuous than that on the stiffness linearity of the CMNSM. Hence, this parameter is selected properly to improve the value of negative stiffness during the design procedure.

3.1.3 Effect of the radial gap λ (Group-1)

Figure 9(a) shows the stiffness curve broadens with the

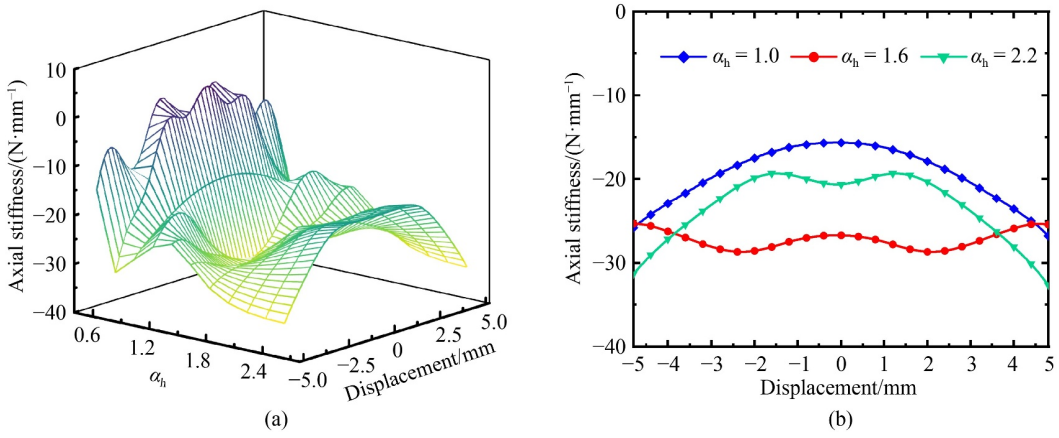

Fig. 7 Effect of α_h on the stiffness of the combined magnetic negative stiffness mechanism: (a) 3D view and (b) 2D view.

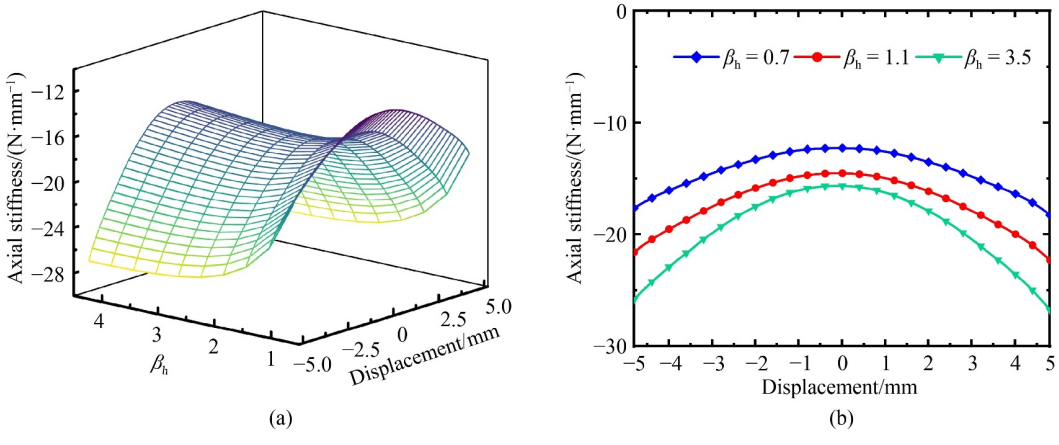

Fig. 8 Effect of β_h on the stiffness of the combined magnetic negative stiffness mechanism: (a) 3D view and (b) 2D view.

growth of radial gap (λ), and the nonlinearity of axial stiffness of the CMNSM improves slightly by increasing λ. Moreover, the value of negative stiffness decreases with the increase of λ due to the increase of magnetic leakage, as shown in Fig. 9(b). The effect of λ on the stiffness of the CMNSM is similar to the effect of β_h, and the value of stiffness and volume of MQZS-VI should be considered during the design procedure.

3.1.4 Effect of the ratio α_v (Group-2)

By increasing H_3 to lower $\alpha_v = H_0/H_3$, the value of stiffness increases, as shown in Fig. 10. The stiffness linearity is improved slightly with the decrease of α_v. Overall, this parameter plays the same role as β_h during the design procedure, which can be selected to improve the value of negative stiffness.

3.1.5 Effect of the ratio β_v (Group-2)

Figure 11 describes the effect of $\beta_v = T_1/T_3$ on the stiffness characteristic. The value of the negative stiffness at the equilibrium position increases first and then descends with the increase of β_v. In addition, this parameter has an enormous influence on the stiffness linearity. An exceedingly small or large β_v can improve the stiffness linearity but lower the stiffness value, so this parameter should be selected in conjunction with other parameters that affect the stiffness linearity to broaden the linear interval of the CMNSM.

3.1.6 Effect of the axial gap L (Group-2)

Figure 12(a) shows axial gap (L) has a substantial effect on the linear interval of negative stiffness. When the axial gap is small, the stiffness curve is like an "arch", which fluctuates greatly from the middle to the sides, which is the same as the common MNSM in an attractive configuration. With the axial gap increasing, the linear interval would be enlarged. The stiffness curve transfers to like an "arch-bridge", whose sides become gentle. However, Fig. 12(b) shows the value of negative stiffness evidently decreases because of the increase of magnetic leakage. When determining this parameter, the width of

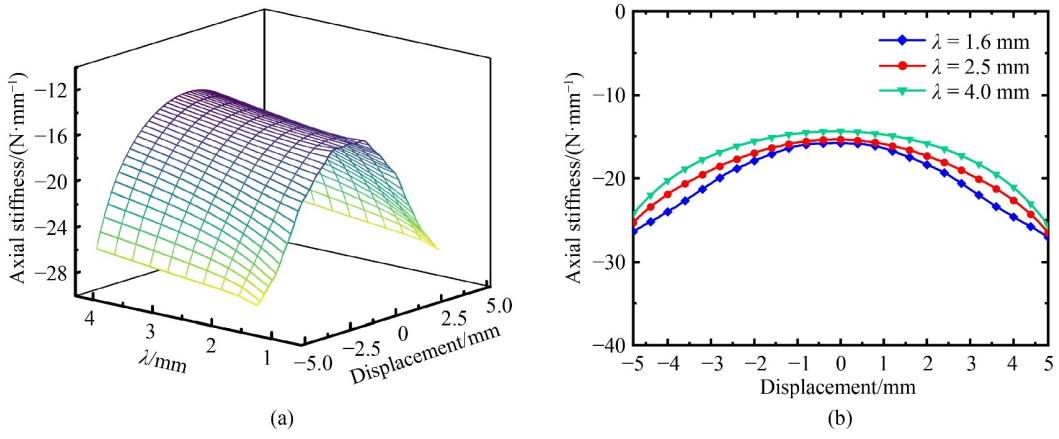

Fig. 9 Effect of λ on the stiffness of the combined magnetic negative stiffness mechanism: (a) 3D view and (b) 2D view.

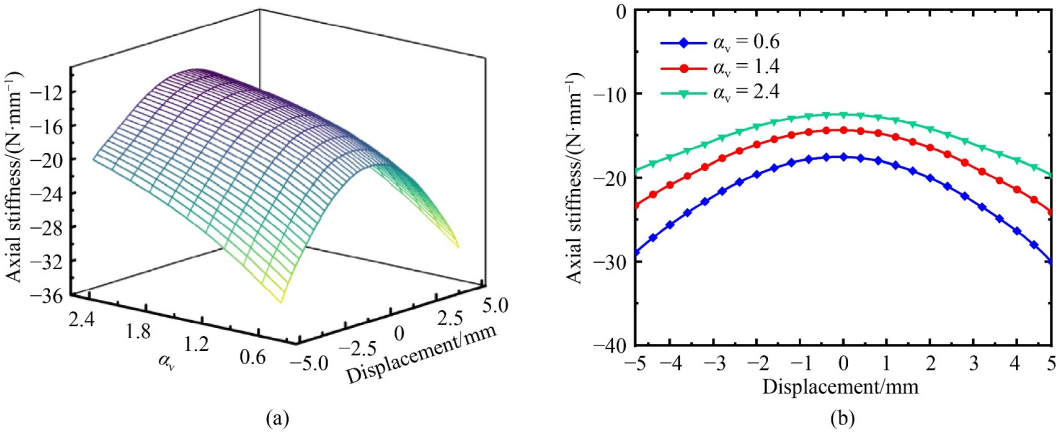

Fig. 10 Effect of α_v on the stiffness of the combined magnetic negative stiffness mechanism: (a) 3D view and (b) 2D view.

the linear interval of negative stiffness needs to be weighed against the value of negative stiffness. The volume factor should also be considered during the design procedure.

3.1.7 Effect of the inside gap of moving magnets ι

The inside gap of moving magnets (ι) is also a vital parameter of the CMNSM, and its effect on stiffness characteristics is shown in Fig. 13. In this paper, the inside gap (ι) is expanded by reducing the axial lengths of the top–bottom moving magnet (H_0). Figure 13(a) shows the fluctuating range of negative stiffness narrows gradually with the growth of ι within a certain range. The amplitude of stiffness is almost constant near the equilibrium position, but the stiffness away from the equilibrium position decreases with the rise of ι, as shown in Fig. 13(b). In addition, the linearity of negative stiffness can be improved by increasing this parameter properly, but increasing ι extremely may lead to the sides of the stiffness curve curling up, which is counterproductive to designing the linear interval of negative stiffness.

3.2 Effect of the geometric parameters on the damping characteristic

Damping coefficient is also an important parameter of the MQZS-VI and is controlled by damping gap (δ), the kinematic viscosity (γ) of the damping fluid, radius (R_p), and the height (H_p) of the piston. The type of flow comprises differential pressure flow and shear flow, and their total discharge of the fluid (W_v) are expressed directly based on the existing study [56]:

$$W_v = W_1 - W_2 = \frac{\pi(2R_p+u)u\delta^{\frac{2u+1}{u}}}{2(2u+1)}\left(\frac{\Delta p}{2\rho\gamma H_p}\right)^{\frac{1}{u}} - \frac{\pi(2R_p+\delta)\delta v}{2}, \quad (13)$$

where W_1 and W_2 are the flow rates of the differential pressure flow and the shear flow, respectively, u is the flow index of the fluid, which is equal to 1 when the fluid belongs to Newtonian fluid, and ρ is the density of the damping fluid. The relationship between pressure difference Δp and damping force F_v can be expressed as

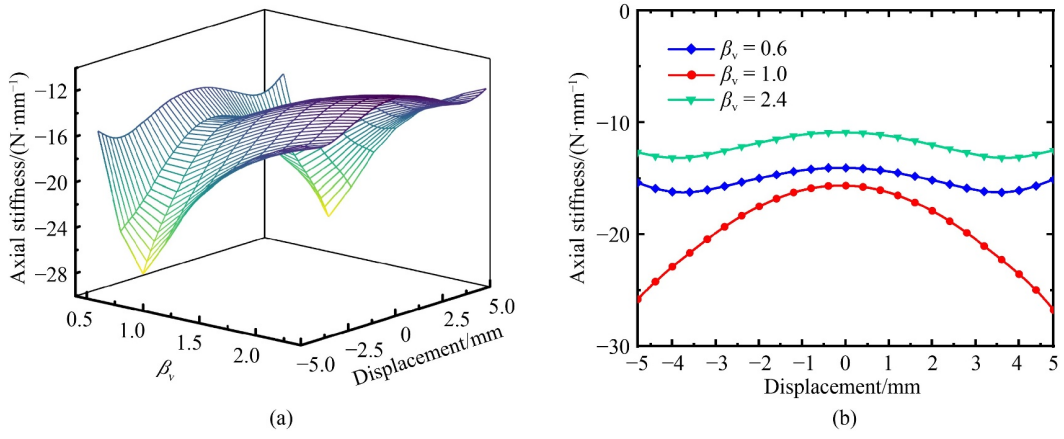

Fig. 11 Effect of β_v on the stiffness of the combined magnetic negative stiffness mechanism: (a) 3D view and (b) 2D view.

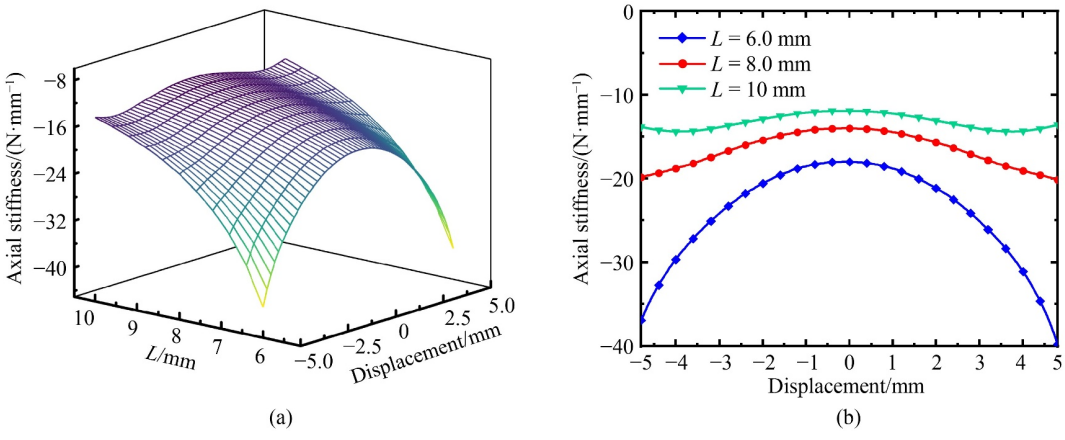

Fig. 12 Effect of L on the stiffness of the combined magnetic negative stiffness mechanism: (a) 3D view and (b) 2D view.

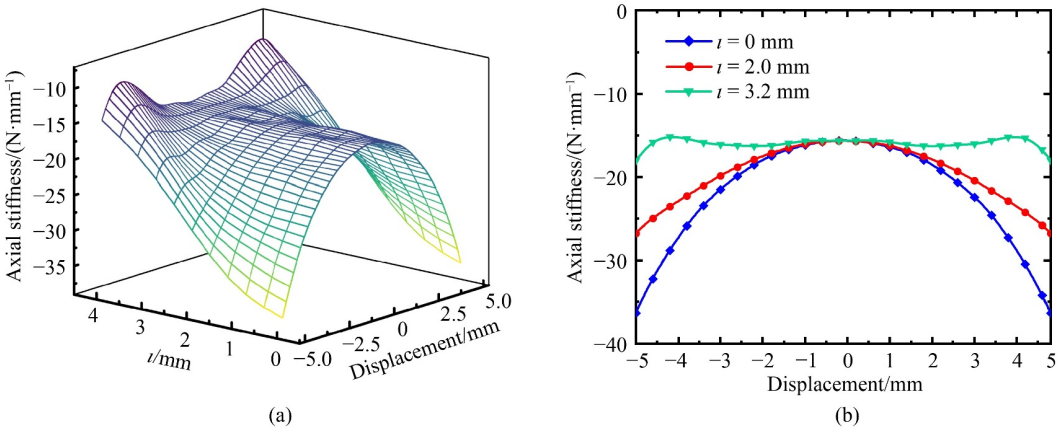

Fig. 13 Effect of ι on the stiffness of the combined magnetic negative stiffness mechanism: (a) 3D view and (b) 2D view.

$$\Delta p = \frac{F_{\mathrm{v}}}{A} = \frac{F_{\mathrm{v}}}{\pi R_{\mathrm{p}}^2}, \tag{14}$$

where subscript "v" indicates that the parameter is related to velocity, and A is the effective surface area of the piston motion. The flow rate of volume change by moving velocity of the piston (v) is equal to the total discharge of the fluid W_{v}.

$$Av = W_{\mathrm{v}}. \tag{15}$$

Substituting Eqs. (13) and (14) into Eq. (15), the axial damping force F_{v} can be obtained:

$$F_{\mathrm{v}} = \frac{2\rho\gamma\pi R_{\mathrm{p}}^2 H_{\mathrm{p}}}{\delta^{2u+1}}\left(\frac{(2u+1)\left(2R_{\mathrm{p}}\delta+\delta^2+2R_{\mathrm{p}}^2\right)}{(2R_{\mathrm{p}}+\delta)u}\right)^u v^u, \tag{16}$$

where γ is the kinematic viscosity of the damping fluid. Then, damping coefficient c is

$$c = \frac{\mathrm{d}F_{\mathrm{v}}}{\mathrm{d}v} = \frac{2\rho\gamma\pi R_{\mathrm{p}}^2 H_{\mathrm{p}} u}{\delta^{2u+1}}\left(\frac{(2u+1)\left(2R_{\mathrm{p}}\delta+\delta^2+2R_{\mathrm{p}}^2\right)}{(2R_{\mathrm{p}}+\delta)u}\right)^u v^{u-1}. \tag{17}$$

Silicone oil is adopted to the damping fluid, its density is 960 kg/m^3, and the fluid index is u = 1 because of the characteristic of Newtonian fluid [56]. The piston rod is in simple harmonic motion at a circular frequency of 1 rad/s, whose amplitude is 5 mm. The damping coefficient is calculated according to Eq. (17), and the relative results are shown in Fig. 14. The damping coefficient reduces nonlinearly with the enlargement of damping gap (δ) but grows linearly with increasing kinematic viscosity (γ), as shown in Fig. 14(a). Figure 14(b) demonstrates that the damping coefficient increases with the rise of the radius (R_{p}) and height (H_{p}) of the piston. The relationship between the damping coefficient and the height of the piston (H_{p}) is also linear, but its effect on the value of the damping coefficient is less conspicuous than that of other parameters.

In conclusion, these parametric studies are important to designing the MQZS-VI, and the following rules are summarized. First, α_{h} and L remarkably determine the linearity of negative stiffness. This linearity can also be improved by increasing ι and β_{v} at the cost of descending the value of negative stiffness. Second, the maximum

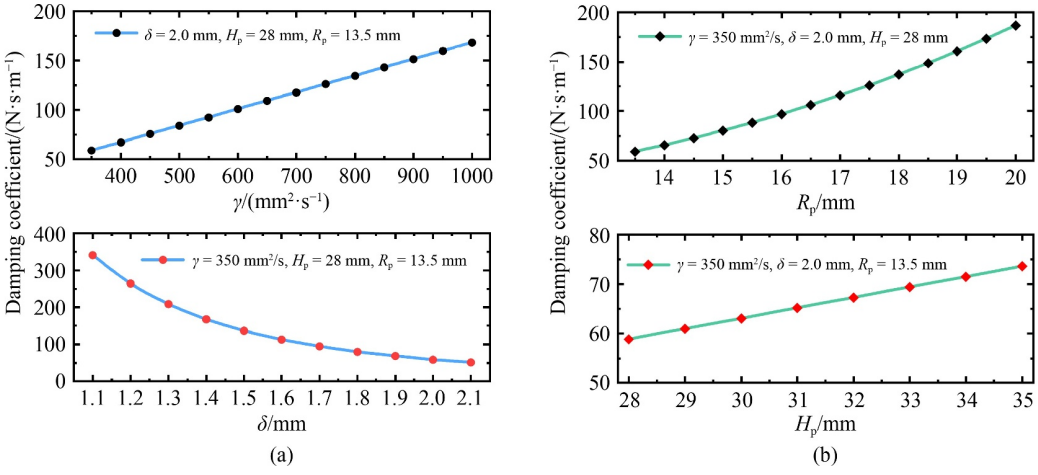

Fig. 14 Effect of geometric parameters and viscosity on damping coefficient: damping coefficients versus (a) δ and γ and (b) R_{p} and H_{p}.

negative stiffness that the CMNSM can generate is determined from B_r, β_h, α_v, and λ. In addition, the damping coefficient can be obtained by matching δ, γ, R_p, and H_p. Finally, the volume of the MQZS-VI also depends on these geometric parameters. Matching appropriate parameters to enhance the isolating performance should also consider the spatial limitation in practical engineering. Manufacturing costs and difficulty should also be considered during the design procedure.

3.3 Design procedure

According to the parametric study on the stiffness and damping characteristics, the design procedure of the MQZS-VI can be obtained. The proposed MQZS-VI is composed of the damping structure and the CMNSM. The following dimensional limitations are required to avoid structure interference:

$$\begin{cases} H_2 \leqslant H_1 < H_p, \\ H_1 + 2L + 2H_3 \leqslant H_c, \\ 2H_0 + 2\iota < H_1, \\ \delta < \lambda, \\ T_1 + r_i < R_p, \\ \lambda + T_2 + r_i + T_1 \leqslant R_c, \\ r_i + T_3 \leqslant R_p + \delta, \end{cases} \tag{18}$$

where H_c and R_c are determined by specific application scenarios. In this paper, the extent of stiffness nonlinearity η is presented as

$$\eta(z) = \left| \frac{k_n(z) - k_{n0}}{k_{n0}} \right|, \tag{19}$$

where k_{n0} is the negative stiffness at the equilibrium position, and $k_n(z)$ is the negative stiffness when the axial displacement is z. Additionally, the design objectives for MQZS-VI are

$$\begin{cases} |k_{n0}/k_p| \approx \varepsilon_{ideal} < 1, \\ \eta(z)_{max} \leqslant \eta_{ideal},\ z \in [-\kappa/2,\ \kappa/2], \\ c \approx c_{ideal}, \end{cases} \tag{20}$$

where ε_{ideal}, c_{ideal}, and η_{ideal} are the ideal values of stiffness counteraction ratio, damping coefficient, and stiffness nonlinearity, respectively, and κ is the design width of the linear-stiffness interval of the CMNSM, which is also called QZS interval because of high counteraction rate for negative stiffness and high linearity of positive stiffness. Its positive stiffness is denoted as k_p. The primary target of design optimization is to broaden the QZS interval, which is to broaden the linear interval of negative stiffness. Its underlying mechanism is combining the stiffness curves of the attractive magnetic negative stiffness mechanism and the repulsive magnetic negative stiffness mechanism reasonably by matching the proper geometric parameters of subsystems of the CMNSM according to the superposition theorem of magnetic fields, which can realize a flat stiffness curve in certain ranges.

Figure 15 shows the design flowchart, which consists of two blocks. The first block is to design the negative stiffness characteristic. In Stage 1, the initial parameters for the MQZS-VI are selected according to the dimensional limitations. The linear interval of stiffness is designed first: Group-1 of the CMNSM should be in repulsive configuration first by adjusting α_h, and the stiffness curve of Group-2 of the CMNSM in attractive configuration is matched to broaden the linear interval of the CMNSM by properly selecting L and β_v. In addition,

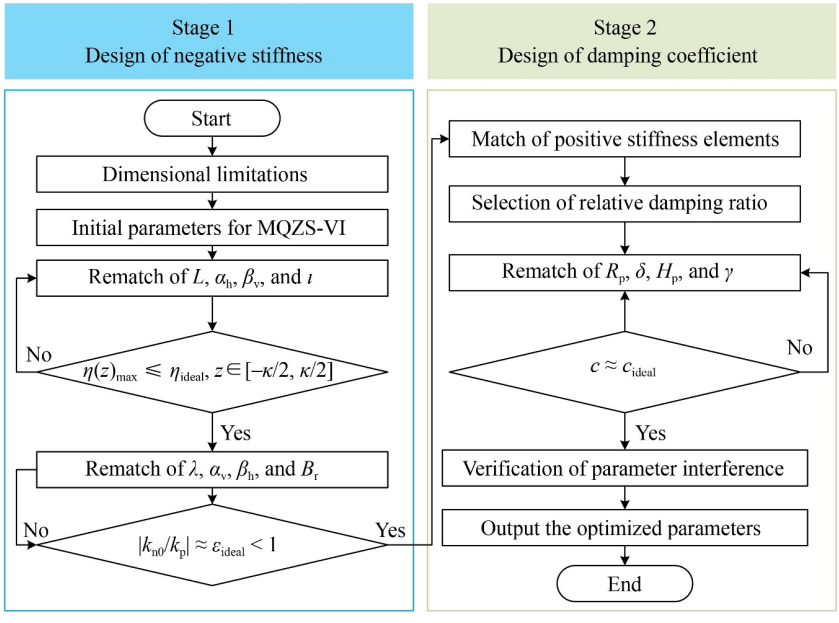

Fig. 15 Design flowchart for the modular quasi-zero stiffness vibration isolator.

matching ι can improve the linear-stiffness interval further. Therefore, after reaching most of the design objectives by selecting L and α_h, ι is optimized to accomplish the goal. At this stage, the negative stiffness at the equilibrium position cannot attain the expected target in general. The stiffness counteraction is not sufficient, which can be improved by adjusting λ, α_v, β_h, and B_r. In Stage 2, the total stiffness is obtained by matching related positive stiffness elements, and then the relative damping ratio can be determined. The damping coefficient is designed by selecting damping gap (δ), the height of the piston (H_p), the radius of the piston (R_p), and kinematic viscosity (γ), avoiding inducing overdamping effect. Finally, verification of all the parameter interference is conducted and provides reliable support for the subsequent design of details.

3.4 Advantages of the optimized MQZS-VI

The novel CMNSM is the key part of the MQZS-VI. The high vibration isolation performance of the MQZS-VI also depends on the advantages of the CMNSM primarily. In this section, the magnitude at the equilibrium position and the extent of the nonlinearity of the novel CMNSM with optimized parameters and the typical CMNSM with ring magnets, which has the same parametric variables as the novel CMNSM, are compared. Differentiated from the novel CMNSM, all the magnets of the typical CMNSM are magnetized axially in the same direction [57]. Similarly, the design space is specified as R_c = 25 mm and H_c = 60 mm.

Figure 16 compares the extent of nonlinearity in the working interval between the novel CMNSM and the typical CMNSM while the value of negative stiffness at the equilibrium position stays the same. The optimized parameters of the novel CMNSM and the typical CMNSM are shown in Table 2. The nonlinearity of the novel CMNSM is smaller than that of the typical CMNSM, especially for the position far from the equilibrium. Figure 16(b) shows the width of the linear interval of the novel CMNSM is 9 mm, which is 50% broader than that of the typical CMNSM if η_{ideal} = 1.0%.

To investigate the advantage of the proposed MQZS-VI in the dynamic characteristic aspect, a QZS vibration isolation system with a single DOF is established by making a positive-stiffness structure parallel to the novel CMNSM, as shown in Fig. 17. m is the mass of the payload, k_p and k_n denote the positive stiffness and the negative stiffness, respectively, and z_b and z_p are the displacements of the base excitation and the payload platform, respectively.

The achieved expressions of axial force and stiffness are integral that is not convenient for the analysis of dynamic equation, which can be approximated by fitting the stiffness curve in Fig. 16(a). The positive stiffness is designed to be 25 N/mm. The axial force (F_z) can be approximated by the 7th-order polynomial as

$$F_z = (k_p + k_n)z = k_0 z + k_1 z^3 + k_2 z^5 + k_3 z^7 = \sum_{i=0}^{3} k_i z^{2i+1}, \quad (21)$$

where k_i $(i = 0,1,\ldots,3)$ are the fitted coefficients. Accordingly, the total stiffness (k_z) is

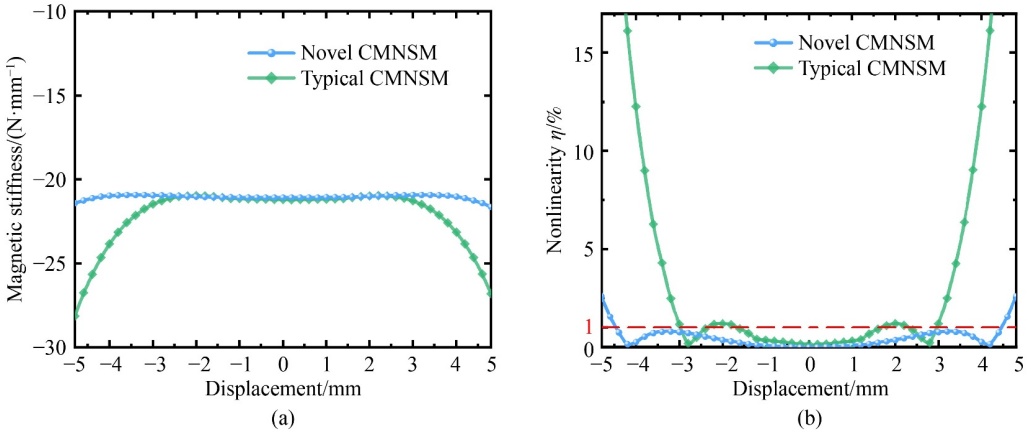

Fig. 16 Comparison of the extent of nonlinearity under the same value of negative stiffness at the equilibrium position: (a) stiffness characteristic and (b) nonlinearity. CMNSM: combined magnetic negative stiffness mechanism.

Table 2 Optimized parameters of CMNSMs

CMNSM type	T_1/mm	H_1/mm	r_i/mm	B_r/T	α_h	β_h	λ/mm	α_v	β_v	L/mm	ι/mm
Novel CMNSM	7.0	26	5.0	1.4	1.0	1.4	4.0	1.0	1.0	9.0	2.5
Typical CMNSM	7.0	26	5.0	1.4	1.0	1.4	5.5	1.0	1.0	7.0	2.0

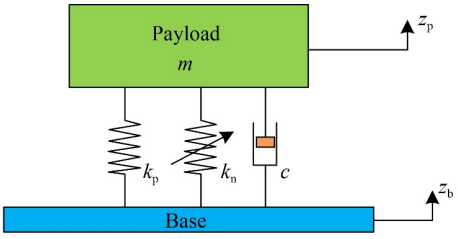

Fig. 17 Dynamic model of quasi-zero stiffness vibration isolation system.

$$k_z = -\frac{F_z}{z} = -k_0 - 3k_1 z^2 - 5k_2 z^4 - 7k_3 z^6 = -\sum_{i=0}^{3}(2i+1)k_i z^{2i}. \tag{22}$$

The dynamic formula of the vibration system can be represented by

$$m\ddot{z}_p + c(\dot{z}_p - \dot{z}_b) + (k_p + k_n)(z_p - z_b) = 0. \tag{23}$$

Equation (21) is substituted into Eq. (23), $z = z_p - z_b$ denotes the relative displacement, and the dynamic formula can be rewritten as

$$m\ddot{z} + c\dot{z} + \sum_{i=0}^{3} k_i z^{2i+1} = -m\ddot{z}_b. \tag{24}$$

The natural frequency (ω_0) of the system is

$$\omega_0 = \sqrt{k_e/m}, \tag{25}$$

where k_e is the stiffness of the system at the equilibrium position.

The base displacement excitation is

$$z_b = Z_b \cos(\omega t), \tag{26}$$

where t is time, and Z_b and ω are the magnitude and circular frequency of the base displacement, respectively.

Defining the nondimensional time as $\tau = \omega_0 t$, the nondimensional dynamic equation can be

$$\ddot{x} + 2\xi\dot{x} + \sum_{i=0}^{3}\alpha_i x^{2i+1} = \Omega^2\cos(\Omega\tau), \tag{27}$$

where $\Omega = \dfrac{\omega}{\omega_0}$, $\xi = \dfrac{c}{2m\omega_0}$, $x = \dfrac{z}{Z_b}$, $\alpha_i = \dfrac{k_i}{k_0}Z_b^{2i}$, $(\cdot) = \dfrac{\mathrm{d}(\cdot)}{\mathrm{d}\tau} = \dfrac{1}{\omega_0}\dfrac{\mathrm{d}(\cdot)}{\mathrm{d}t}$. Ω is the nondimensional frequency, ξ is the relative damping ratio, and x is the nondimensional displacement.

The formula can be solved by the harmonic balance method when assuming the steady-state solution is

$$x = X\cos(\Omega\tau + \varphi), \tag{28}$$

where X is magnitude of the nondimensional displacement and substituting Eq. (28) into Eq. (27) yields

$$\begin{cases} -X\Omega^2 + \Pi = \Omega^2\cos\varphi, \\ -2\xi X\Omega = \Omega^2\sin\varphi, \end{cases} \tag{29}$$

where

$$\Pi = \sum_{i=0}^{3}\frac{C_{2i+1}^{i+1}}{2^{2i}}\alpha_i X^{2i+1} = \alpha_0 X + \frac{3}{4}\alpha_1 X^3 + \frac{5}{8}\alpha_2 X^5 + \frac{35}{64}\alpha_3 X^7. \tag{30}$$

Squaring and adding Eq. (29), the amplitude–frequency relationship is

$$(X^2 - 1)\Omega^4 + (4\xi^2 X^2 - 2\Pi X)\Omega^2 + \Pi^2 = 0. \tag{31}$$

The displacement of the payload platform is given by

$$z_p = z_b + z = Z_b\cos(\omega t) + Z_b X\cos(\Omega\tau + \varphi). \tag{32}$$

Then, the displacement transmissibility of the isolator is

$$T_d = \left|\frac{z_p}{z_b}\right| = \left|\frac{\cos(\omega t) + X\cos(\Omega\tau + \varphi)}{\cos(\omega t)}\right| = \sqrt{X^2 + 2X\cos\varphi + 1}. \tag{33}$$

By substituting Eq. (29) into Eq. (33), the transmissibility can be rewritten as

$$T_d = \sqrt{X^2 + 1 + \frac{-2X^2\Omega^2 + 2X\Pi}{\Omega^2}} = \sqrt{\frac{\Omega^2 + 2X\Pi - X^2\Omega^2}{\Omega^2}}. \tag{34}$$

The approximate solutions of the total axial force and stiffness are calculated and agree with the accurate solutions, especially in the equilibrium position, as shown in Fig. 18(a). The coefficients of the seventh-order polynomial are given in Table 3.

The transmissibility can be calculated by Eq. (34), the mass of payload is 15 kg, and relative damping ratio is set to 0.3 because of the existence of fluid damping. The effect of disturbance displacement on the vibration isolation performance of the MQZS-VI is investigated, as shown in Fig. 18(b). The natural frequency increases with the rise of disturbance displacement, but the phenomenon is slight because of the high linearity of the novel CMNSM and damping fluid structure in the MQZS-VI. The excitation amplitude during a certain scope has minor effects on the dynamic characteristic proposed MQZS-VI.

4 Experimental validations

To validate the performance of the MQZS-VI, an experimental prototype was designed to investigate its static and dynamic characteristics. To reduce the influence of the relative permeability on experiments, the isolator was made of stainless steel, whose relative permeability is close to that of air. The small-scale manufacture of a magnetic ring with radiative magnetization was expensive, so it was built by splicing 12 radially magnetized arc magnets in this paper. All the magnets were made of neodymium magnets of N38. Silicone oil was selected to supply the damping force, and the metal spring with 60Si2Mn was designed. All the design parameters of the prototype are listed in Table 4.

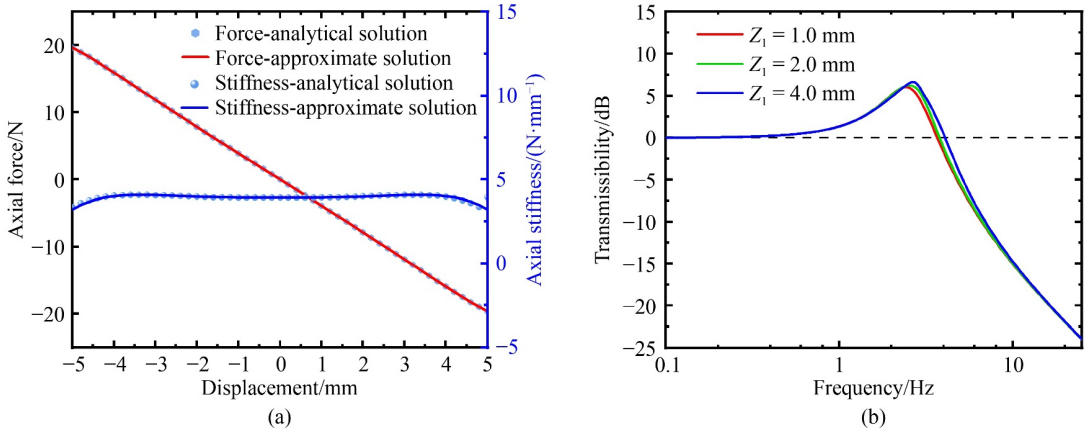

Fig. 18 Characteristics of quasi-zero stiffness vibration isolation system with the proposed modular quasi-zero stiffness vibration isolator: (a) approximate force–displacement and stiffness–displacement curves and (b) transmissibility with different disturbance displacement.

Table 3 Coefficients of the seventh-order polynomial

Case	k_0	k_1	k_2	k_3
MQZS-VI	−3.91 N/mm	-4.49×10^{-2} N/mm^3	-3.25×10^{-4} N/mm^5	1.88×10^{-5} N/mm^7

4.1 Setup of static experiments

To measure the axial force of the MQZS-VI, the static experimental system depicted in Fig. 19 was established. The system was made of a hydraulic universal testing machine (MTS Exceed 43.504, MTS Industrial System Co., Ltd., Shenzhen Branch, Shenzhen, China) and an industrial computer. The signals of force and displacement were obtained by the corresponding sensors integrated into the universal testing machine, and then all the measured signals were processed on the industrial computer. The static experiments were made of two parts. First, the stiffness of the metal spring was identified by experiment to guarantee the QZS characteristic of the prototype. Then, the MQZS-VI was compressed with different preloads to validate its supporting capacity and stiffness characteristic. All the compressive experiments were repeated three times to verify the validity of the data.

Table 4 Design parameters of the prototype

Component	Parameter	Value
CMNSM	Aggregate of axial length of moving magnets, H_1	26 mm
	Axial length of the middle static magnet, H_2	26 mm
	Axial length of the top moving magnet, H_0	5 mm
	Axial length of the top stator magnet, H_3	5 mm
	Thickness of the moving magnet, T_1	7.5 mm
	Thickness of the middle stator magnet, T_2	5 mm
	Thickness of the top stator magnet, T_3	7.5 mm
	Radial gap, λ	4 mm
	Axial gap, L	9 mm
	Inside gap of moving magnets, ι	2 mm
	Inner radius of the moving magnet, r_i	5 mm
Metal spring	Wire diameter, d	6 mm
	Middle diameter, D	75 mm
	Free height, H	75 mm
	Effective turn number, n_0	2.15
Silicone oil	Kinematic viscosity, γ	350 mm^2/s
	Height of the piston, H_p	28 mm
	Radius of the piston, R_p	13.5 mm
	Damping gap, δ	2 mm

According to the experimental results of the metal spring and the vibration isolator, the novel CMNSM of MQZS-VI could be obtained and validated.

4.2 Results of static experiments

The average force–displacement curves are shown in Fig. 20(a). The static characteristic of the MQZS-VI was constant with the preload increasing, but the curve became rough due to the friction. The maximum supporting force of the metal spring could reach 600 N according to its size and material characteristics, which could substantially improve the loading capacity of the MQZS-VI by optimizing the preloading structure. The relevant stiffness–displacement curves were fitted by fifth-order polynomial to obtain information clearly. Fitted stiffness–displacement curves are shown in Fig. 20(b). The stiffness value of metal spring is 13.8 N/mm, whereas the average value of the stiffness at the equilibrium position (z = 0) is 1.51 N/mm due to the existence of CMNSM. This result means about 90% of the positive stiffness is counteracted. With the growth of preload, the stiffness of MQZS-VIs would increase slightly because large preload may induce that the piston rod inclined slightly during the compressive experiments, which would introduce more friction stiffness in the MQZS-VI.

To validate the analytical model of magnetic force, the force and stiffness of the novel CMNSM were obtained and compared with theoretical solution. Figure 21(a) shows the force–displacement curve of the CMNSM was obtained by subtracting the force–displacement curve of metal spring from that of the MQZS-VI. The experimental results agree with the theoretical ones. The absolute errors of force and stiffness are shown in Fig. 21(b). The root mean square (RMS) of force error is 1.51 N, and that of stiffness error is 0.93 N/mm, which may be caused by the dimensional machining error of the prototype or the inhomogeneity of the actual magnetization of magnets. The proposed analytical model of the novel CMNSM was validated, and it can be utilized to design the MQZS-VI.

4.3 Setup of dynamic experiments

To validate the dynamic characteristic of the MQZS-VI, an experimental prototype was designed, as depicted in

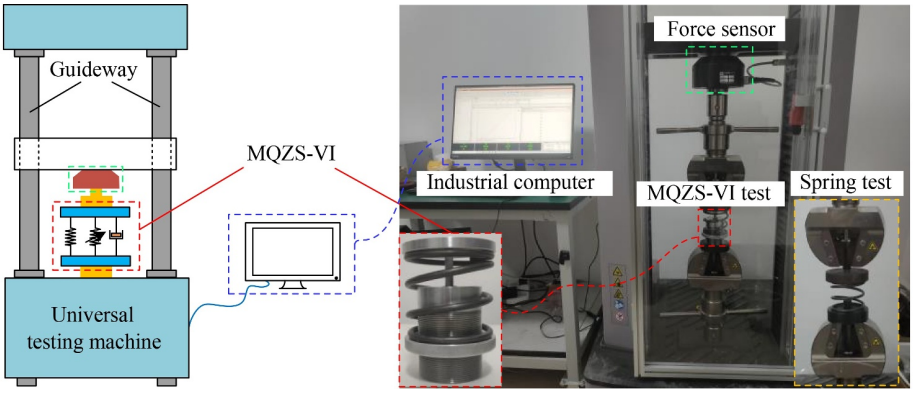

Fig. 19 Experimental system of static characteristics. MQZS-VI: modular quasi-zero stiffness vibration isolator.

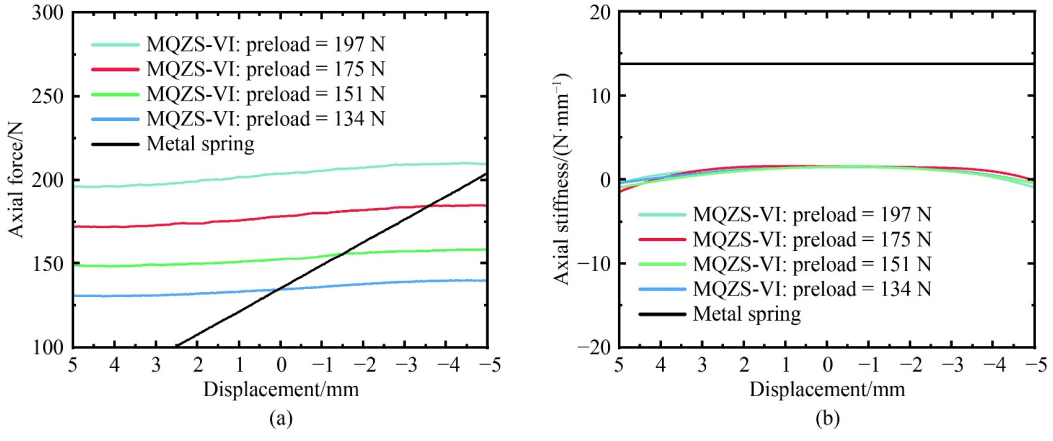

Fig. 20 Results of the static experiments with different preload: (a) force–displacement curve and (b) fitted stiffness–displacement curves by 5th-order polynomial. MQZS-VI: modular quasi-zero stiffness vibration isolator.

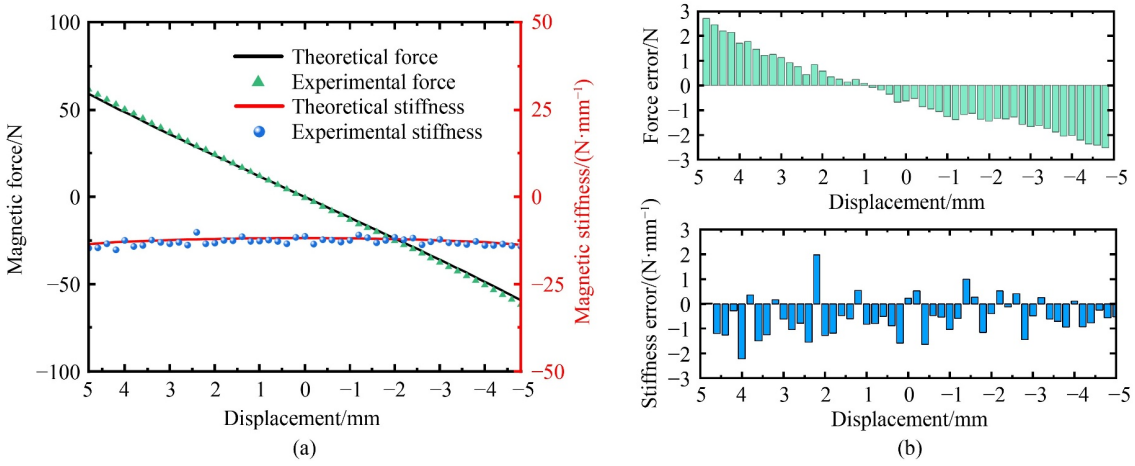

Fig. 21 Validation of the analytical model: (a) axial magnetic force and stiffness of the combined magnetic negative stiffness mechanism versus the displacement and (b) experimental error.

Fig. 22. The bottom of the cylinder block was mounted on a marble base, while the central piston rod was fixed on a crossbeam supported and guided by an air-bearing guide to ensure vertical-only movement with a near-zero friction force. The marble base was fixed on a pneumatic platform, which was connected to the ground by air springs. The experimental system mainly comprised a controller (Lenovo Rescuer 15-ISK, Lenovo Information Products Co., Ltd., Guangzhou, China), a dynamic signal analyzer (Spider-20, Hangzhou Radiant Digital Technology Co., Ltd., Hangzhou, China), a power amplifier (MB 500VI, MB Dynamics GmbH, Krefeld, Germany), DC power (LRS 100-24, Mean Well Enterprises Co., Ltd., Taipei, China), velocity sensors (VSE-15D-6, Tokyo Sokushin Co., Ltd., Tokyo, Japan), and an exciter (Modal 110, MB Dynamics GmbH, Krefeld, Germany). The bandwidth of the exciter was 0–5000 Hz, and the velocity sensor (VSE-15D-6) can measure signals as low as 0.2 Hz, so vibration responses below 1 Hz can be evaluated better. The controller sent the ideal excitation information to the dynamic signal analyzer. It transferred the relative information to the electric signal and output to the power amplifier, and then the exciter would start to work. The velocity sensors were used to measure the vibration signals of the base and payload, whose energy was supplied by DC power. The measured signal would be processed by a dynamic signal analyzer and output to the controller. All the signals were then visualized in a data acquisition window on the controller.

The mass of the payload was 15.47 kg, which included the upper velocity sensor. In addition, the piston rod in the MQZS-VI was replaced with another piston rod without any magnet to build a prototype of a spring damper without the CMNSM. Comparing the experimental results with the theoretical results would validate the convince of data. Moreover, the advantage of the MQZS-VI would be confirmed by comparing its results with the experimental results of the spring damper without

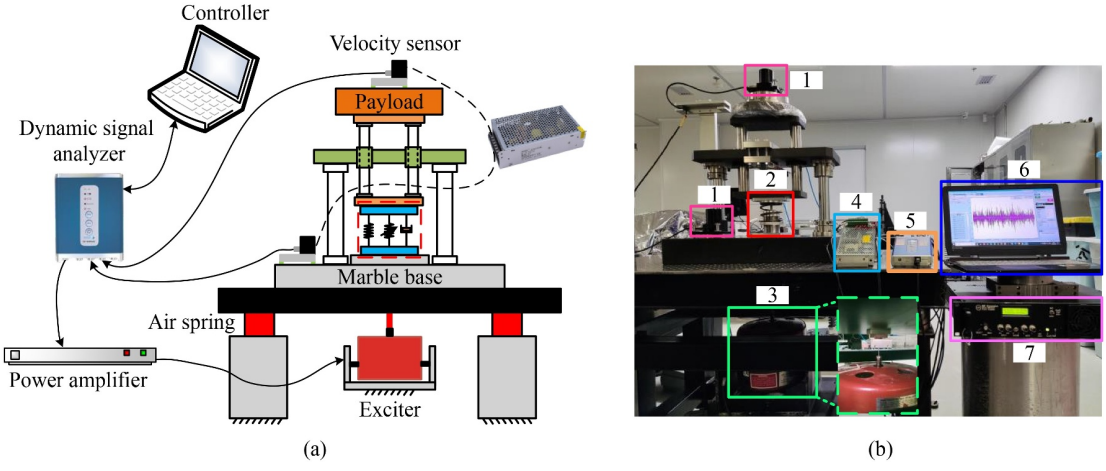

Fig. 22 Experimental system of dynamic characteristics: (a) schematic diagram and (b) photo. 1–Velocity sensor, 2–Modular quasi-zero stiffness vibration isolator prototype, 3–Exciter, 4–DC power, 5–Dynamic signal analyzer, 6–Controller, 7–Power amplifier.

CMNSM. To simulate the real vibration environment, the random signal was adopted as the output of the exciter. The frequency range was 0.3–100.0 Hz, and the RMS of the random signal was 3.96×10^{-3} m/s^2 due to the limitation of the actual performance of the exciter, whose maximum force was 500 N.

4.4 Results of dynamic experiments

The experimental results in the time domain are shown in Fig. 23(a). The vibration response of the MQZS-VI is lower than that of the spring damper without the CMNSM. The attenuation rate of vibration is denoted P, which is presented as

$$P=\frac{\left|\mathrm{RMS}(\dot{z}_{\mathrm{b}})-\mathrm{RMS}(\dot{z}_{\mathrm{p}})\right|}{\mathrm{RMS}(\dot{z}_{\mathrm{b}})}\times100\%. \tag{35}$$

The RMS of the vibration velocity of the base is 0.1014 mm/s and the responses of the payload with two kinds of vibration isolation systems in Table 5 show the attenuation rate of vibration could reach 90% by utilizing the proposed MQZS-VI.

Table 5 Vibration response in the time domain

Type of vibration isolation systems	RMS of response velocity/(mm·s^{-1})	Attenuation rate/%
Without the CMNSM	0.0889	12.32
With the CMNSM	0.0101	90.04

Figure 23(b) shows the theoretical solutions agree with the experimental results in general, illustrating the validity of experimental data. The blue curve shows an apparent resonance peak occurs at 4.82 Hz, and the natural frequency of the MQZS-VI (red curve) is 1.46 Hz. Table 6 shows the initial frequency of vibration isolation (transmissibility is equal to 0 dB) is decreased from 6.8 to 2.0 Hz, almost $\sqrt{2}$ times the natural frequency. In addition, compared with the spring damper without the CMNSM, the proposed MQZS-VI has an advantage in restraining the resonance peak, which is because the relative damping ratio rises with the decrease of natural frequency while the damping coefficient is constant.

Hence, the MQZS-VI demonstrates a better isolation performance. The isolation bandwidth can be improved by enhancing the preload force to increase the mass of the rated load or to increase the residual flux density to counteract more positive stiffness. The natural frequency of the system can be less than 1 Hz by increasing the mass of the load, which is of great importance. In addition, the resonance peak of the MQZS-VI is lower than that of the spring damper without the CMNSM under the same experimental condition because the relative damping ratio increases with the decrease of stiffness if the other parameters are unchanged. The advantages of the MQZS-VI over the spring damper without the CMNSM are demonstrated when they are utilized for the dynamic loaded equipment, especially under the strict requirement of vibration isolation with small mounting space.

5 Conclusions

A novel MQZS-VI with damping was proposed in this paper, which was realized by highly integrating the novel CMNSM into the damping structure, so that the

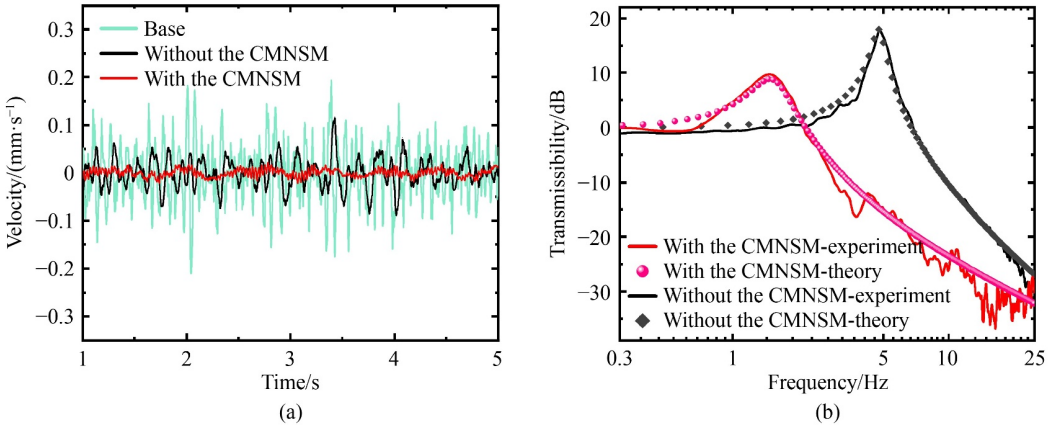

Fig. 23 Results of the dynamic experiments: (a) response of velocity and (b) transmissibility. CMNSM: combined magnetic negative stiffness mechanism.

Table 6 Transmissibility in the frequency domain

Type of vibration isolation systems	Natural frequency/Hz	Initial frequency of isolation/Hz	Resonance peak/dB
Without the CMNSM	4.82	6.8	17.74
With the CMNSM	1.46	2.0	9.79

contradiction between the strict mounting space and high-performance isolation would be improved in the vibration isolation of dynamic loaded. An analytical model of the interaction force with composite magnetization direction, including axial and radiative directions, was also proposed and then validated. The effects of geometric parameters on the stiffness and damping characteristics of MQZS-VI were revealed, and then the design procedure was proposed. During the design procedure, the stiffness and damping coefficient can be matched dependently, which reduced the complexity of parameter matching compared with negative stiffness dampers. Moreover, the QZS interval of optimized MQZS-VI was wider than that of the QZS vibration isolators with typical CMNSM. Finally, static and dynamic experiments were conducted on a prototype of the proposed MQZS-VI. The correctness of the proposed analytical model and the high-performance vibration isolation ability were validated. The isolation frequency band was extended because the natural frequency was reduced from 6.8 (without the CMNSM) to 2.0 Hz (with the CMNSM). In addition, by refining the design of the preloaded structure, the effective payload capacity of the MQZS-VI can reach 600 N, which meant the natural frequency of the system can be reduced to below 1 Hz. The novel MQZS-VI has a bright application prospect in dynamic loaded equipment due to the wide QZS interval, high damping characteristics, compact volume, low complexity of parameter matching, and modular design.

In addition, the MQZS-VIs can be combined to establish a Stewart platform to study the multiple-DOF isolation performance, which will be conducted in the near future. Thus, the configuration and application of MQZS-VI deserves further research to serve the vibration isolation for dynamic loaded equipment better.

Nomenclature

Abbreviations

CMNSM	Combined magnetic negative stiffness mechanism
DOF	Degree-of-freedom
FEA	Finite element analysis
MNSD	Magnetic negative stiffness damper
MNSM	Magnetic negative stiffness mechanism
MQZS-VI	Modular quasi-zero stiffness vibration isolator
QZS	Quasi-zero stiffness
RMS	Root mean square

Variables

A	Effective surface area of the piston motion
B_r	Residual flux density
B_r^c, B_r^q	Magnitudes of radial magnetic flux density generated by the equivalent current loop and magnetic charge loop, respectively
B_z^c, B_z^q	Magnitudes of axial magnetic flux density generated by the equivalent current loop and magnetic charge loop, respectively
$\boldsymbol{B}^\mathrm{c}$, $\boldsymbol{B}^\mathrm{q}$	Magnetic flux densities generated by the equivalent current loop and the magnetic charge loop, respectively
$\boldsymbol{B}_\mathrm{r}^\mathrm{c}$, $\boldsymbol{B}_\mathrm{r}^\mathrm{q}$	Radial magnetic flux densities generated by the equivalent current loop and the magnetic charge loop, respectively
$\boldsymbol{B}_z^\mathrm{c}$, $\boldsymbol{B}_z^\mathrm{q}$	Axial magnetic flux densities generated by the equivalent current loop and the magnetic charge loop, respectively
c	Damping coefficient
c_ideal	Ideal damping coefficient
d	Wire diameter of the metal spring
D	Middle diameter of the metal spring
E	Complete elliptic integral of the second kind
F_v	Damping force
F_z	Axial force
F_z^* (* = u, m, l)	Axial force of moving magnets suffered from the top stator, the middle stator, and the lower stator respectively
F_{zc}^c, F_{zc}^q	Forces of the current loop acted by another current loop and another magnetic charge loop, respectively
F_{zq}^c, F_{zq}^q	Forces of the magnetic charge loop acted by another current loop and another magnetic charge loop, respectively
G	Complete elliptic integral of the first kind
H	Free height of the metal spring
H_0, H_3	Axial lengths of the moving magnets and the stator magnets on the top–bottom side, respectively
H_1	Axial length of the assemble moving magnet
H_2	Axial length of the middle stator magnet
H_c	Axial height of design space
H_p	Height of the piston head
$I_{i\mathrm{b}}$	Current of the inner current loop of the bottom moving magnet (i = 1) or the bottom stator magnet (i = 3)
$I_{i\mathrm{u}}$	Current of the inner current loop of the upper moving magnet (i = 1) or the upper stator magnet (i = 3)
$I_{j\mathrm{b}}$	Current of the outer current loop of the bottom moving magnet (j = 2) or the bottom stator magnet (j = 4)
$I_{j\mathrm{u}}$	Current of the outer current loop of the upper moving magnet (j = 2) or the bottom stator magnet (j = 4)

I_m, I_s	Surface currents of the equivalent current loop of the moving magnet and the stator magnet with radiative magnetization, respectively
$\boldsymbol{J}_l$ (l = 1,2,…,4)	Surface density of the equivalent ampere's currents of the magnets with axial magnetization
k_e	Stiffness of the vibration isolation system at equilibrium position
k_i (i = 0,1,…,3)	Fitted coefficients of the nonlinear axail force
k_n	Negative stiffness
k_{n0}	Negative stiffness at the equilibrium position
$k_n(z)$	Negative stiffness when the axial displacement is z
k_p	Positive stiffness
k_z	Total stiffness
L	Axial gap between the moving magnets and stator magnets on the top–bottom side
m	Mass of the payload
M_i (i = 1,2,…,4)	Magnitude of magnetization of the magnet
$\boldsymbol{M}_i$ (i = 1,2,…,4)	Magnetization of the magnet
n_0	Effective turn number of the metal spring
N_b (b = c, v, s)	Number of segments for fictitious current loops, volume magnetic charge loops, and surface magnetic charge loops, respectively
$\boldsymbol{n}_k$ (k = 1,2,…,8)	Unit vector normal to the surface of the ring magnets
P	Attenuation rate of vibration
Δp	Pressure difference
Q_m, Q_s	Magnetic charges of the equivalent magnetic charge loop of the moving magnet and the stator magnet with axial magnetization, respectively
Q_{si}	Magnetic charge of the micro unit of the equivalent inner surface magnetic charge loop of the middle moving magnet (i = 1) or the middle stator magnet (i = 3)
Q_{sj}	Magnetic charge of the micro unit of the related outer surface magnetic charge loop of the middle moving magnet (j = 2) or the middle stator magnet (j = 4)
Q_{vk}	Value of the magnetic charge of the micro unit of the equivalent volume magnetic charge loop of the middle moving magnet (k = 1) or the middle stator magnet (k = 3)
r_1, r_2	Inner and outer radii of the moving magnet, respectively
r_3, r_4	Inner and outer radii of the middle stator magnet, respectively
r_5, r_6	Inner and outer radii of the upper-bottom stator magnet, respectively
r_i	Inner radius of all the magnets apart from the middle stator magnet
r_m	Radial coordinate of micro units of equivalent loops of the moving magnet
r_s	Radial coordinate of micro units of equivalent loops of the stator magnet
r_{vk}, r_{vp}	Radii of the equivalent volume magnetic charge loops of the middle stator magnet and the middle moving magnet, respectively
R_c	Radius of design space
R_p	Radius of the piston head
$\boldsymbol{r}$	Radial unit vector
t	Time
T_1, T_3	Thicknesses of all the moving magnets and the stator magnets on the top–bottom side, respectively
T_2	Thickness of the middle stator magnet
T_d	Displacement transmissibility of the isolator
u	Flow index of the fluid
v	Moving velocity of the piston
W_1, W_2	Flow rates of the differential pressure flow and the shear flow, respectively
W_v	Total discharge of the fluid
x	Nondimensional displacement
X	Magnitude of the nondimensional displacement
z	Relative axial displacement
z_1, z_2	Axial coordinates of the lower plane of the upper stator magnet and the upper moving magnet, respectively
z_{1u}, z_{2t}	Axial coordinates of the current loop of the upper stator magnet and the upper moving magnet, respectively
z_3, z_4	Axial coordinates of the lower plane of the middle stator magnet and the middle moving magnet, respectively
z_{3n}, z_{4i}	Axial coordinates of the surface magnetic charge loop of the middle stator magnet and the middle moving magnet, respectively
z_5, z_6	Axial coordinates of the lower plane of the lower moving magnet and the lower stator magnet, respectively
z_{5q}, z_{6w}	Axial coordinates of the current loop of the lower moving magnet and the lower stator magnet, respectively
z_b, z_p	Displacements of the base excitation and the payload platform, respectively
z_m	Axial coordinate of micro units of equivalent loops of the moving magnet
z_p (p = 1,2,…,6)	Axial coordinate of the lower plane of each magnet
z_s	Axial coordinate of micro units of equivalent loops of the stator magnet
z_{vj}, z_{vm}	Axial coordinates of the volume magnetic charge loop of the middle stator magnet and the middle moving magnet
Z_b	Magnitude of the base displacement
$\boldsymbol{z}$	Axial unit vector

α_h	Ratio of H_1 to H_2
α_v	Ratio of H_0 to H_3
β_h	Ratio of T_1 to T_2
β_v	Ratio of T_1 to T_3
η	Extent of stiffness nonlinearity
η_{ideal}	Ideal stiffness nonlinearity
κ	Design width of the linear-stiffness interval of the CMNSM
ρ	Density of the damping fluid
γ	Kinematic viscosity of the damping fluid
δ	Damping gap
ι	Distance between the middle moving magnet and the top–bottom moving magnets
λ	Radial gap between the moving magnets and middle stator magnet
μ_0	Permeability of the vacuum
ε_{ideal}	Ideal stiffness counteraction ratio
$\boldsymbol{\theta}$	Circumferential unit vector
ω	Circular frequency
ω_0	Natural frequency
τ	Nondimensional time
ξ	Relative damping ratio
ψ	Variable of integration
φ	Phase of nondimensional displacement
Ω	Nondimensional frequency

Acknowledgements This work was supported by the National Key R&D Program of China (Grant Nos. 2020YFB2007300 and 2020YFB2007601), the National Natural Science Foundation of China (Grant Nos. 52075193, 52305107, and 52275112), the National Science and Technology Major Project of China (Grant No. 2017ZX02101007-002), and the Postdoctoral Science Foundation of China (Grant No. 2022M711250).

Electronic Supplementary Material The supplementary material can be found in the online version of this article at https://doi.org/10.1007/s11465-023-0778-7 and is accessible to authorized users.

Conflict of Interest The authors declare that they have no conflict of interest.

References

1. Wang B, Jiang Z, Hu P D. Study on 6-DOF active vibration-isolation system of the ultra-precision turning lathe based on GA-BP-PID control for dynamic loads. Advances in Manufacturing, 2023 (in press)
2. Ikeda K, Kamimori K, Kobayashi I, Kuroda J, Uchino D, Ogawa K, Endo A, Kato T, Liu X J, Peeie M H B, Kato H, Narita T. Basic study on mechanical vibration suppression system using 2-degree-of-freedom vibration analysis. Vibration, 2023, 6(2): 407–420
3. Demir M H. Design and analysis of passive components-supported SLS-VI mechanism for the control of road-induced stretcher vibrations during ambulance movement. Journal of Vibration Engineering and Technologies, 2022, 11(8): 3959–3979
4. Lin F C, Zheng H, Xiang B, Xu R, Jiang W, Lang L. Vibration-induced noise in extremely low frequency magnetic receiving antennas. IEEE Antennas and Wireless Propagation Letters, 2021, 20(6): 913–917
5. Dong G X, Ma C C, Zhang F, Luo Y J, Bi C X. Non-resonant response of the novel airborne photoelectric quasi-zero stiffness platform with friction damping. International Journal of Applied Electromagnetics and Mechanics, 2020, 64(1–4): 315–324
6. Jiang S, Wang J Z, Wang S K, Shen W. Vibration isolation control performance for an innovative 3-DOF parallel stabilization platform. Journal of Mechanical Science and Technology, 2022, 36(7): 3677–3689
7. Liu H Z, Huang X Z, Yan M, Chang M X. Dynamic response and time-variant reliability analysis of an eight-rod shock isolator. Proceedings of the Institution of Mechanical Engineers, Part C: Journal of Mechanical Engineering Science, 2022, 236(13): 7041–7054
8. Shin Y, Moon S, Jung W, Bae S. Experimental approach to active mounts using electromagnetic actuator and rubber with consideration of shock resistance for naval shipboard equipment. Shock and Vibration, 2019, 2019: 3958359
9. Qu D, Liu X D, Liu G T, He T. Vibration isolation characteristics and control strategy of parallel air spring system for transportation under abnormal road and eccentric load conditions. Measurement and Control, 2021, 54(3–4): 252–268
10. Li S H, Feng G Z, Zhao Q. Design and research of semiactive quasi-zero stiffness vibration isolation system for vehicles. Shock and Vibration, 2021, 2021: 5529509
11. Li H, Li Y C, Li J C. Negative stiffness devices for vibration isolation applications: a review. Advances in Structural Engineering, 2020, 23(8): 1739–1755
12. Zhao Y M, Cui J N, Zou L M. Genetic optimization of repulsive magnetic array negative stiffness structure for high-performance precision micro-vibration isolation. Journal of Vibration Engineering and Technologies, 2022, 10(4): 1325–1336
13. Lu Z Q, Liu W H, Ding H, Chen L Q. Energy transfer of an axially loaded beam with a parallel-coupled nonlinear vibration isolator. Journal of Vibration and Acoustics, 2022, 144(5): 051009
14. Wu J L, Zeng L Z, Han B, Zhou Y F, Luo X, Li X Q, Chen X D, Jiang W. Analysis and design of a novel arrayed magnetic spring with high negative stiffness for low-frequency vibration isolation. International Journal of Mechanical Sciences, 2022, 216: 106980
15. Zhao J L, Zhou G, Zhang D Z, Kovacic I, Zhu R, Hu H Y. Integrated design of a lightweight metastructure for broadband vibration isolation. International Journal of Mechanical Sciences, 2023, 244: 108069
16. Wang Q, Zhou J X, Wang K, Lin Q D, Xu D L, Wen G L. A compact quasi-zero-stiffness device for vibration suppression and energy harvesting. International Journal of Mechanical Sciences, 2023, 250: 108284
17. Wang Q, Zhou J X, Xu D L, Ouyang H J. Design and experimental investigation of ultra-low frequency vibration isolation during neonatal transport. Mechanical Systems and Signal Processing,

2020, 139: 106633
18. Ma Z Z, Zhou R P, Yang Q C. Recent advances in quasi-zero stiffness vibration isolation systems: an overview and future possibilities. Machines, 2022, 10(9): 813
19. Jing X J, Chai Y Y, Chao X, Bian J. *In-situ* adjustable nonlinear passive stiffness using X-shaped mechanisms. Mechanical Systems and Signal Processing, 2022, 170: 108267
20. Abuabiah M, Dabbas Y, Herzallah L, Alsurakji I H, Assad M, Plapper P. Analytical study on the low-frequency vibrations isolation system for vehicle's seats using quasi-zero-stiffness isolator. Applied Sciences, 2022, 12(5): 2418
21. Zhao F, Ji J C, Ye K, Luo Q T. Increase of quasi-zero stiffness region using two pairs of oblique springs. Mechanical Systems and Signal Processing, 2020, 144: 106975
22. Zhao F, Ji J C, Ye K, Luo Q T. An innovative quasi-zero stiffness isolator with three pairs of oblique springs. International Journal of Mechanical Sciences, 2021, 192: 106093
23. Wei C Y. Design and analysis of a novel vehicle-mounted active QZS vibration isolator. Iranian Journal of Science and Technology, Transactions of Mechanical Engineering, 2023, 47(4): 2121–2131
24. Chen Z B, Yu S B, Wang B, Zhuang X Y, Lin F. The research about application of quasi-zero stiffness vibration isolation technology in a large vehicle-mounted optic-electronic equipment. Ain Shams Engineering Journal, 2023, 14(2): 101841
25. Meng K, Sun Y, Pu H Y, Luo J, Yuan S J, Zhao J L, Xie S R, Peng Y. Development of vibration isolator with controllable stiffness using permanent magnets and coils. Journal of Vibration and Acoustics, 2019, 141(4): 041014
26. Wu J L, Che J X, Chen X D, Jiang W. Design of a combined magnetic negative stiffness mechanism with high linearity in a wide working region. Science China Technological Sciences, 2022, 65(9): 2127–2142
27. Zhang Y, Liu Q H, Lei Y G, Cao J Y, Liao W H. Halbach high negative stiffness isolator: modeling and experiments. Mechanical Systems and Signal Processing, 2023, 188: 110014
28. Yuan S J, Sun Y, Wang M, Ding J H, Zhao J L, Huang Y N, Peng Y, Xie S R, Luo J, Pu H Y, Liu F Q, Bai L, Yang X D. Tunable negative stiffness spring using maxwell normal stress. International Journal of Mechanical Sciences, 2021, 193: 106127
29. Tu L X, Ning D H, Sun S S, Li W X, Huang H, Dong M M, Du H P. A novel negative stiffness magnetic spring design for vehicle seat suspension system. Mechatronics, 2020, 68: 102370
30. Zhang F, Xu M L, Shao S B, Xie S L. A new high-static-low-dynamic stiffness vibration isolator based on magnetic negative stiffness mechanism employing variable reluctance stress. Journal of Sound and Vibration, 2020, 476: 115322
31. Wang M T, Su P, Liu S Y, Chai K, Wang B X, Lu J F. Design and analysis of electromagnetic quasi-zero stiffness vibration isolator. Journal of Vibration Engineering and Technologies, 2023, 11(1): 153–164
32. Wang T, Zhu S Q. Resonant frequency reduction of vertical vibration energy harvester by using negative-stiffness magnetic spring. IEEE Transactions on Magnetics, 2021, 57(9): 1–7
33. Wu M K, Wu J L, Che J X, Gao R Q, Chen X D, Li X Q, Zeng L Z, Jiang W. Analysis and experiment of a novel compact magnetic spring with high linear negative stiffness. Mechanical Systems and Signal Processing, 2023, 198: 110387
34. Yan B, Yu N, Wu C Y. A state-of-the-art review on low-frequency nonlinear vibration isolation with electromagnetic mechanisms. Applied Mathematics and Mechanics, 2022, 43(7): 1045–1062
35. Zhao Y M, Cui J N, Zou L M, Cheng Z Y. Modeling and dynamics of magnetically repulsive negative stiffness permanent magnetic array for precision air/magnetic composite vibration isolation. International Journal of Structural Stability and Dynamics, 2022, 22(7): 2250031
36. Zheng Y S, Li Q P, Yan B, Luo Y J, Zhang X N. A Stewart isolator with high-static-low-dynamic stiffness struts based on negative stiffness magnetic springs. Journal of Sound and Vibration, 2018, 422: 390–408
37. Hao R B, Lu Z Q, Ding H, Chen L Q. Orthogonal six-DOFs vibration isolation with tunable high-static-low-dynamic stiffness: experiment and analysis. International Journal of Mechanical Sciences, 2022, 222: 107237
38. Hao R B, Lu Z Q, Ding H, Chen L Q. Shock isolation of an orthogonal six-DOFs platform with high-static-low-dynamic stiffness. Journal of Applied Mechanics, 2023, 90(11): 111004
39. Diez-Jimenez E, Rizzo R, Gómez-García M J, Corral-Abad E. Review of passive electromagnetic devices for vibration damping and isolation. Shock and Vibration, 2019, 2019: 1250707
40. Yang X F, Yan L, Shen Y J, Li H C, Liu Y L. Dynamic performance analysis and parameters perturbation study of inerter–spring–damper suspension for heavy vehicle. Journal of Low Frequency Noise, Vibration and Active Control, 2021, 40(3): 1335–1350
41. Guan D, Cong X J, Li J, Wang P B, Yang Z W, Jing X J. Theoretical modeling and optimal matching on the damping property of mechatronic shock absorber with low speed and heavy load capacity. Journal of Sound and Vibration, 2022, 535: 117113
42. Huang X B, Yang B T. Towards novel energy shunt inspired vibration suppression techniques: principles, designs and applications. Mechanical Systems and Signal Processing, 2023, 182: 109496
43. Lu Z Q, Brennan M, Ding H, Chen L Q. High-static−low-dynamic-stiffness vibration isolation enhanced by damping nonlinearity. Science China Technological Sciences, 2019, 62(7): 1103–1110
44. Wu Z M, Li H, Kong X S, Deng Z H. A novel design of vibration isolator with high and frequency dependent damping characteristics based on a large negative Poisson's ratio (LNPR) structure. Mechanical Systems and Signal Processing, 2023, 186: 109818
45. Liu C R, Yu K P, Tang J. New insights into the damping characteristics of a typical quasi-zero-stiffness vibration isolator. International Journal of Non-Linear Mechanics, 2020, 124: 103511
46. Ma H Y, Yan B, Zhang L, Zheng W G, Wang P F, Wu C Y. On the design of nonlinear damping with electromagnetic shunt damping. International Journal of Mechanical Sciences, 2020, 175: 105513
47. Ma R S, Bi K M, Hao H. A novel rotational inertia damper for amplifying fluid resistance: experiment and mechanical model. Mechanical Systems and Signal Processing, 2021, 149: 107313
48. Shi X, Zhu S Y. Simulation and optimization of magnetic negative stiffness dampers. Sensors and Actuators A: Physical, 2017, 259:

14–33

49. Liu W X, Lui E M. Mathematical modeling and parametric study of magnetic negative stiffness dampers. Advances in Structural Engineering, 2020, 23(8): 1702–1714
50. Wang Z H, Cheng Z P, Yin G Z, Shen W A. A magnetic negative stiffness eddy-current inertial mass damper for cable vibration mitigation. Mechanical Systems and Signal Processing, 2023, 188: 110013
51. Ravaud R, Lemarquand G, Lemarquand V. Force and stiffness of passive magnetic bearings using permanent magnets. Part 1: axial magnetization. IEEE Transactions on Magnetics, 2009, 45(7): 2996–3002
52. Ravaud R, Lemarquand G, Lemarquand V. Force and stiffness of passive magnetic bearings using permanent magnets. Part 2: radial magnetization. IEEE Transactions on Magnetics, 2009, 45(9): 3334–3342
53. Kremers M F J, Paulides J J H, Ilhan E, Janssen J L G, Lomonova E A. Relative permeability in a 3D analytical surface charge model of permanent magnets. IEEE Transactions on Magnetics, 2013, 49(5): 2299–2302
54. Vučković A N, Raičević N B, Ilić S S, Aleksić S R. Interaction magnetic force calculation of radial passive magnetic bearing using magnetization charges and discretization technique. International Journal of Applied Electromagnetics and Mechanics, 2013, 43(4): 311–323
55. Vučković A N, Ilić S S, Aleksić S R. Interaction magnetic force calculation of ring permanent magnets using Ampere's microscopic surface currents and discretization technique. Electromagnetics, 2012, 32(2): 117–134
56. Yu Q, Xu D F, Zhu Y, Guan G F, Li Q. Damping characteristic modeling and numerical simulation analysis of the viscous damper of a clearance hydrocylinder. Journal of Vibration and Shock, 2020, 39(20): 161–167
57. Shi X, Zhao F L, Yan Z D, Zhu S Y, Li J Y. High-performance vibration isolation technique using passive negative stiffness and semiactive damping. Computer-Aided Civil and Infrastructure Engineering, 2021, 36(8): 1034–1055